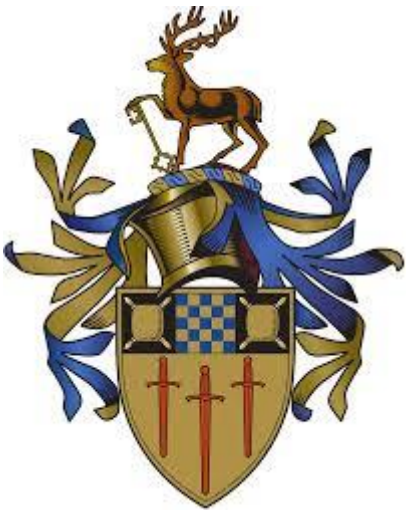

Methods for Measuring the Neutron Detection Efficiency at CLAS12

Jude Christopher Buckley

Department of Physics, University of Surrey, Guildford, GU2 7XH

Submitted to the University of Surrey as partial fulfillment of the master's degree in physics

January 2025

Abstract

Write this AFTER completion…

Declaration of Originality

This dissertation and the work to which it refers are the results of my own efforts. Any ideas, data, images, or text resulting from the work of others (whether published or unpublished) are fully identified as such within the work and attributed to their originator in the text, bibliography, or in footnotes. This dissertation has not been submitted in whole or in part for any other academic degree or professional qualification. I agree that the University has the right to submit my work to the plagiarism detection service TurnitinUK for originality checks. I own the copyrights.

Acknowledgments

I would like to thank my supervisor Professor Gerard P. Gilfoyle for his continued extensive support and guidance before and throughout this research period. I also extend my thanks to Dr Paul Stevenson for providing his assistance as my visiting tutor for the year. Additionally, I would like to express my gratitude towards Lamya Basheen for providing this project and assisting me during it, allowing me to complete the study without issue. Lastly, thank you to the University of Richmond, and the CLAS Collaboration at the Jefferson lab, for providing me with this research opportunity.

List of Abbreviations

NSAC	Nuclear Science Advisory Committee
QCD	Quantum Chromodynamics
GPD	Generalised Parton Distributions
CEBAF	Continuous Electron Beam Accelerator Facility
CLAS12	CEBAF Large Acceptance Spectrometer at 12 GeV
MM	Missing Mass
PMT	Photomultiplier Tube
FT	Forward Trigger
HBT	Hit-based Tracking
TBT	Time-Based Tracking
CND	Central Neutron Detector
CTOF	Central Time of Flight
SVT	Silicon Vertex Tracker
MMT	Micro-Megas Tracker
LTCC	Low Threshold Cherenkov Counter
DC's	Drift Chambers
HTCC	High Threshold Cherenkov Counter
FTOF	Forward Time of Flight
ECAL	Electromagnetic Calorimeter
PCAL	Pre-shower Calorimeter
NDE	Neutron Detection Efficiency
CB	Crystal Ball
DCB	Double Crystal Ball

Contents

Chapter 1.

Introduction

Precis and LRID Reflection

1.1 History of the Jefferson Lab

The Thomas Jefferson Lab (JLAB) is a US Department of Energy-funded National laboratory in Newport News, Virginia. The history of the laboratory culminates many interests proposed by the Nuclear Science Advisory Committee (NSAC) "Long Range Plan" [1] in 1979. It called for a new accelerator facility that satisfied multiple interests within the community: It was argued that an accelerator facility with a high duty factor (~100%) and operation luminosities of 10^{35} $cm^{-2}s^{-1}$ [13] could allow for continuous acceleration of energies greater than 2GeV, stating that this would be significant enough energy to probe internal nucleon structure. A continuous beam satisfied the conditions to perform exclusive and semi-inclusive measurements, making coincidence experiments possible [1]. These specifications enable interactions between scattered products to be

identified, providing deeper studies into elastic and inelastic scattering [2][13]. Facilities such as The Stanford Linear Accelerator Facility (SLAC) could perform acceleration at sufficient energies to investigate this scattering but with current accelerator limitations. SLAC had a lower kinematic range due to the accelerator's linear structure, and could only operate in short bursts, as its low-duty (<1%) factor Linacs would melt under continuous applied current. By 1973, the SLAC group had performed 8 major experiments [3] and sufficient insight into deep inelastic e-p, e-d, and e-n scattering. This confirmed the existence of quark structure within the Nuclear Physics Community, contributing to NSAC's proposition. In 1987, construction of the Continuous Electron Beam Accelerator Facility (CEBAF) began. Since its activation in 1995, the laboratory has performed hundreds of experiments in its four experimental halls. In 2012, CEBAF ceased operation in preparation to upgrade from 6GeV energy maximum to 12GeV. One major modification from this increase is the upgrade of CLAS in Hall B to account for the 12GeV beam energy. The upgrades were completed in December 2017, and experiments

1.2 Physics at CEBAF

In the time around the proposition of the Long-Range Plan, a new theory for Nuclear Strong Interaction known as Quantum Chromodynamics (QCD) had found further success. Non-perturbative QCD describes interacting particles as "single-bound states of permanently confined constituents called quarks" [4] that carry electric charge, with gluons interactions between quarks. Colour-carrying "flux tubes" connect these gluons and determine their interactions. QCD is imperative for assisting pre-existent colour theory, as it states they must remain confined in bound states, allowing for the

important prediction of colour confinement. It was predicted that at higher four-momentum Q^2 (multi-GeV), gluon interactions would become weakened, behaving under free field theory as a liberated quark-gluon plasma. This state would allow for greater observation of the prediction of quark colours and quark confinement [4][5]. A Higher kinematic range, and fully inclusive measurements would provide optimal conditions for observing and extending current QCD distributions [6] and allowing for high Q^2 form factor measurements.

1.3 Nuclear Form Factors

In the non-perturbative regime, the Elastic and Magnetic form factors can describe the spatial distribution of charge, current, and magnetization within nucleons. These form factors provide insight into the scale of nucleon internal structure and the total contributions from each constituent quark [18]. Form Factors are measured from the Fourier transforms of the cross sections of protons and neutrons produced in polarizable electron scattering experiments. The Elastic and Magnetic form factors of the proton (G_M^p, G_E^p) are relatively well-understood, along with the neutron elastic form factor (G_E^n). Measurements of the Neutron Magnetic form factor (G_M^n) provide agreeable values using different methods at low Q^2, yet there is conflict over the value at higher energies. The Jefferson Lab has optimal facilities for extracting the value of G_M^n, an experiment to measure is currently approved. This experiment measures the ratio of inelastic electron-proton (e-p) over electron-neutron (e-n) scattering events and thus requires measuring neutrons.

1.4 Accelerator Facility Overview

CEBAF is a recirculating electron accelerator at JLab, built from the specifications laid out by NSAC in 1979, running with a ~100% duty factor, allowing for continuous acceleration up to 12GeV. A comprehensive layout of CEBAF is shown in Figure 1.41 (See Appendix C for additional plots outlining CEBAF subsystems). A 100keV photocathode within CEBAF's electron gun emits electrons, split into 499MHz bunches by a radio-frequency chopper[12] at an 85% polarization [9]. These bunches are phase separated by 120 degrees, in preparation for arrival at each of the individual halls A, B, C, and D. They are accelerated up to 123MeV within the electron gun and are injected into the Northern

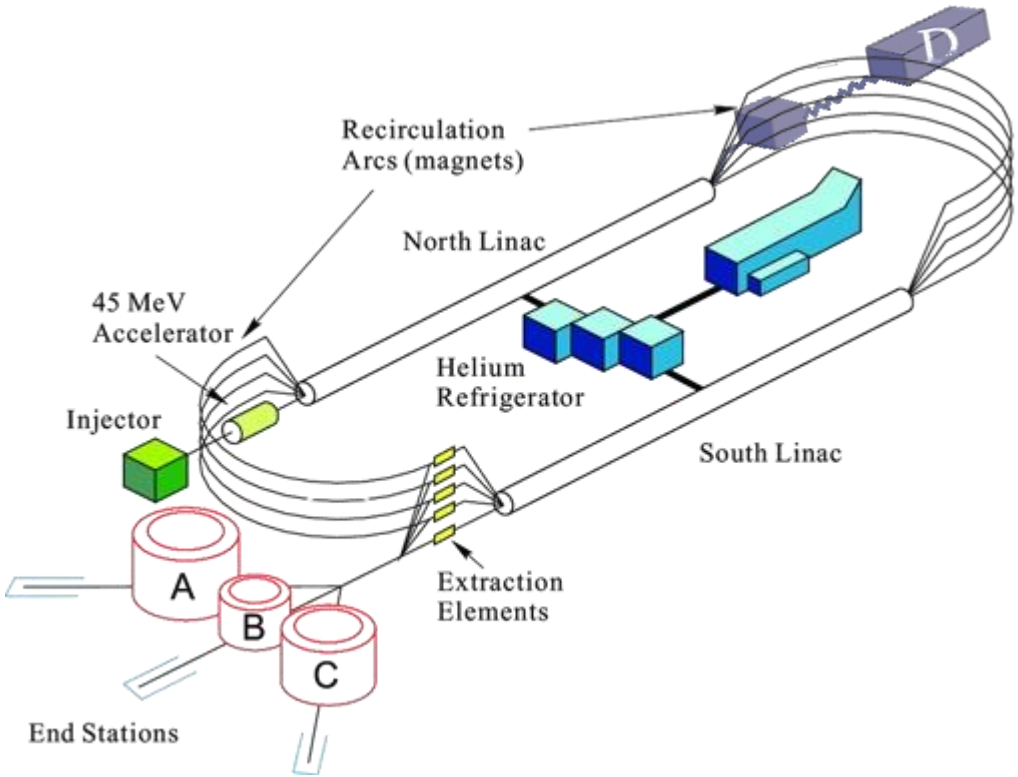

Figure 1.41: Rendition of the Continuous Electron Beam Accelerator Facility (CEBAF). Showing an overview of the general facility structure, a picture from [8], hall D has been edited in for fullness.

Linac to begin recirculation through CEBAF. Two superconducting radiofrequency (SRF) Linacs, north and south, provide electron acceleration of up to 12GeV. Each Linac contains 200 5-cell 1497MHz Niobium cavities, matching the frequency of the electron bunches. Each cell has a length of $\beta\pi/2$, so a magnetic field accelerates electrons applied each half radio frequency period [10][11]. A 17000-gallon refrigerator circulates liquid helium throughout sets of cryo-modules and cryo-units. Between each cryomodule is a set of quadrupole magnets that apply a transverse magnetic field to the electrons, which direct and focus the beam, and assist in retaining a low halo. These various corrective procedures are continuously performed along the Linac, maintaining a high duty factor (~100%), and continuous acceleration by keeping the cavities at a temperature of 2K[11]. Five arc magnet layers are positioned at each Linac's poles and recirculate electrons through the accelerator. Spreading magnets bend electron paths vertically at each Linac's ends and are recombined upon re-entry. The Electrons receive no acceleration through the arcs and all travel at the same speed, independent of energy. Electrons are recirculated through CEBAF up to five times (five and a half for hall D, see figure 1.41), reaching a maximum of 12GeV, at which point a beam switchyard allocates a path to the halls.

1.5 The CLAS12 Detector

Located in Hall B is the CEBAF large acceptance spectrometer at 12GeV (CLAS12). Formally known as CLAS in the 6GeV era, it was constructed upon the 12GeV upgrade in 2016. With a continuous electron beam, the Detector design followed the many major prospects NSAC proposed for deepening the current understanding of nuclear physics: An extension of Hadron and Meson spectroscopy at CLAS12 allows for greater understanding of QCD distributions, confinement, alongside studies of higher mass baryon final states and mesonic states [14]. The Design additionally permits an extension

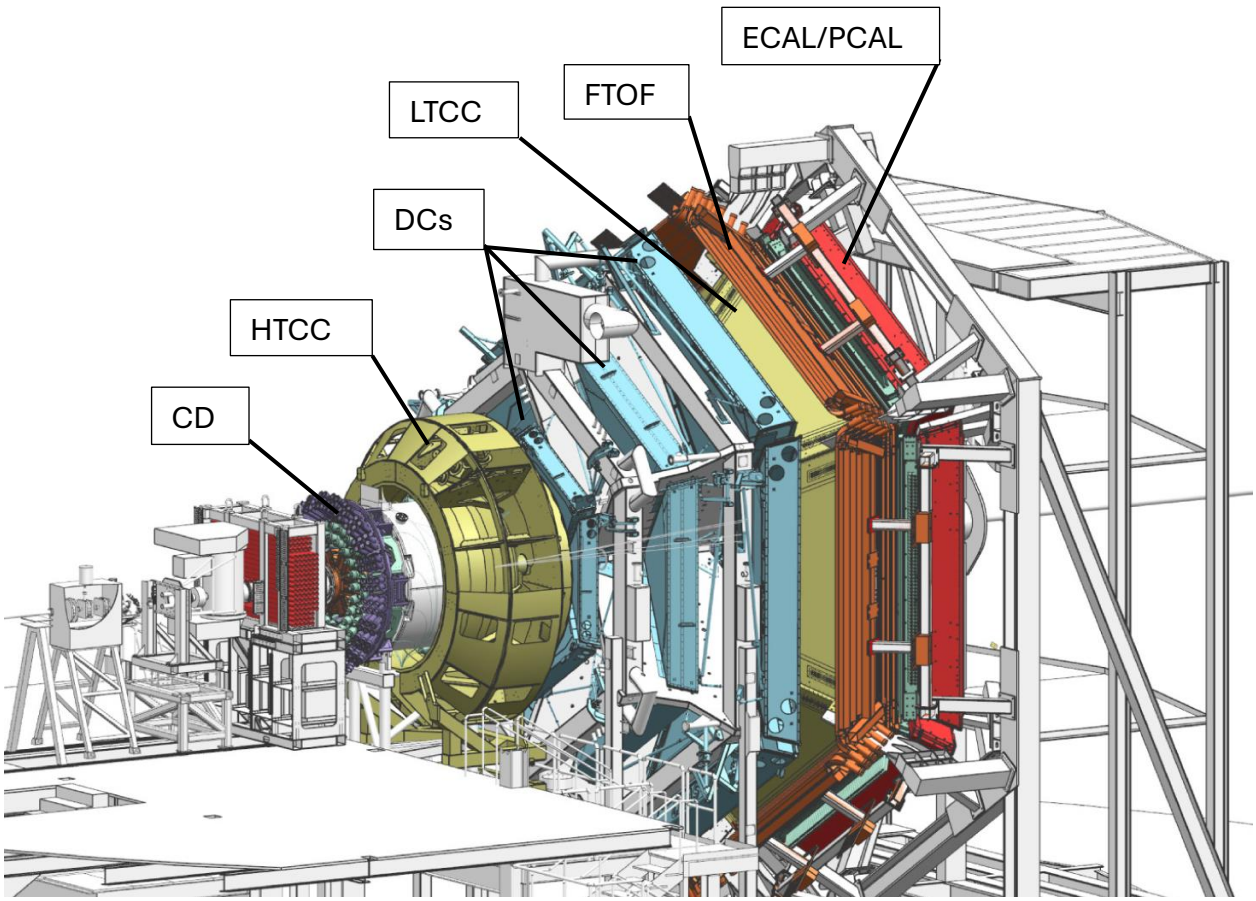

Figure 1.51: Diagram of CLAS12, depictions of each subsystem are shown. Beamline enters from the left, forward detector and central detector placements are shown. Picture from [19], labels are edited in.

of past and current GPD, QCD, and form factor data, due to a higher kinematical range and a greater maximum Q^2. The Detector captures most of the scatter products from an event over a large portion of the 4π solid angle. It is separated into two major sub-systems surrounding a polarizable target: the Central Detector (CD) and the Forward Detector (FD). Two superconducting magnets; a toroid and a solenoid provide a continuous 5T magnetic field that bends the paths of particles through CLAS12, and a zero field is generated around the target to allow for polarization [15].

1.5.1 Central Detector Overview

Electrons that collide in greater proximity to the target nuclei are strongly deflected, and the scatter products spread over greater angles, these are captured by the CD. The CD surrounding the target, covering a polar angle of $35^o < \theta < 135^o$, with 360^o azimuthal angle coverage. This is provided by the CD's Central time-of-flight (CTOF) detector [13], and Central Neutron Detector (CND). These subsystems assist with charged particle identification performed by subsystems in the FD. Tracking in the CD is performed by the Silicon Vertex Tracker (SVT) and the Barrel Micromegas Tracker (BMT), combined into what is known as the Central Vertex Tracker (CVT). Furthermore, a Central Neutron Detector (CND) is placed as the outermost layer to the CD to detect neutrons and other neutral particles with a ~10% efficiency [20].

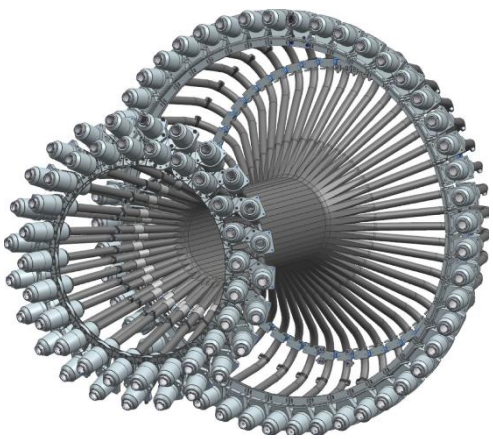

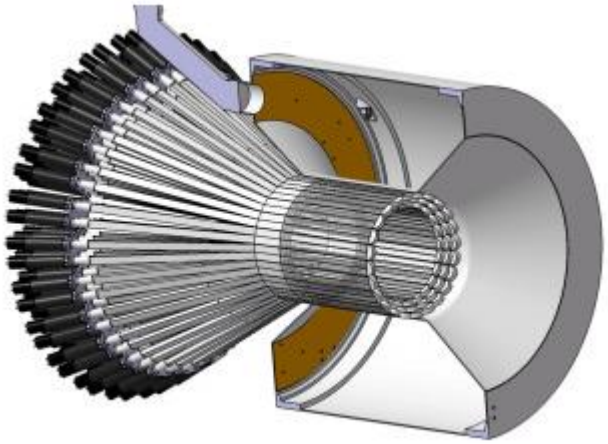

Figures 1.52, 1.53 : CTOF (left), adopted from [13], CND (right) additionally showing the solenoid, adopted from [20]. Figures visualize the polar and azimuthal coverage of the CD. (See Appendix B, figure B.2 for more geometric information)

1.5.2 Forward Detector Overview

As electrons retain their forward momentum, most of the scatter products are weakly deflected by the torus and are captured by the FD. These FD lies farther down the beamline to capture these scatter products, covering a polar angle of $5^{o} < \theta < 45^{o}$. A forward tagger (FT) is used to cover the internal $2.5^{o} < \theta < 4.5^{o}$. Particles that pass through the FD are tracked and identified using 6 subsystems: High/ low Threshold Cherenkov Counters (HTCC/LTCC) and the Forward time-of-flight (FTOF) provide particle identification and timing information in conjunction with the Electromagnetic/Pre-shower Calorimeters (ECAL/PCAL), which also measure energy. In addition, the Ring Imaging Cherenkov Detector (RICH) provides further identification for heavier charged Pions/Kaons with energies > 3GeV [13]. As particles above this energy are discarded by the HTCC and LTCC and cannot be captured by the resolution of the FTOF. Drift Chambers (DCs) track the path that individual charged particles take through the FD and are pivotal for the final reconstruction.

1.5.3 Particle Tracking and Identification

Electron collisions with CLAS12's target create a reaction, where products are scattered throughout the FD and CD. Each product is tracked and identified from data processed by each subsystem, and its path through the detector is reconstructed, named an "event". FD's HTCC. The HTCC spans 5-35° over the polar angle [16] and fully covers the azimuthal angle, and is used to identify electrons, pions, and Kaons at low energies (<3GeV). It utilizes Cherenkov radiation produced by high-speed electrons moving through a CO_2 gas medium and focuses the light through a series of 48 mirror panels. This is collected by light cones into PMTs and processed into a coordinate cluster. Drift Chambers (DC's) are used to reproduce particle tracks and map particle trajectories through the forward detector's toroidal magnetic field. There are three layers of six sector regions, each divided into two superlayers containing 6 sublayers of wires recognized as hexagonal cells. A six-dimensional "cross" is placed between the two superlayers of each of the three DC regions. A distance of closest approach (DOCA) method for each

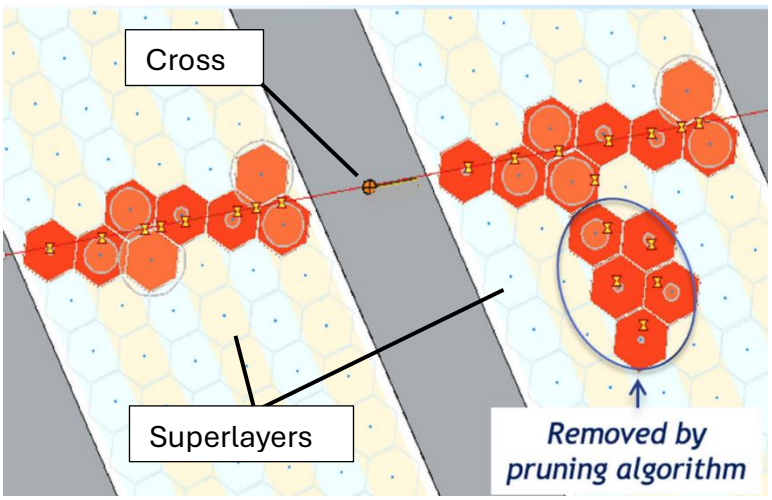

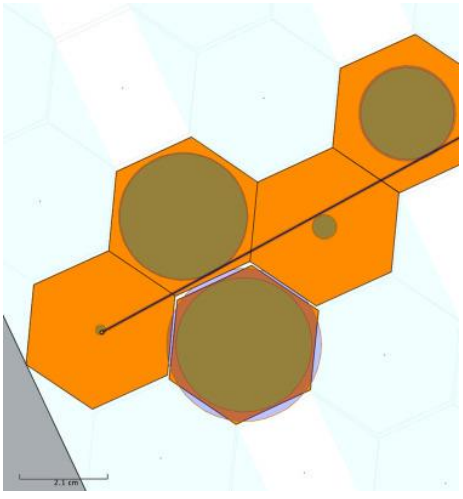

Figures 1.54, 1.55: Superlayer Cross placement and result (left), adopted from [13] and adjusted. Hexagonal wire cross section and DOCA method (right), adopted from [21].

hexagonal wire cross-section is employed to track the path through the superlayers shown in Figures 1.54, and 1.55. This portion of particle tracking incorporates the drift time of electrons through the chambers and is part of CLAS12's Time-Based-Tracking (TBT), (see section 2.1.2). The LTCC mimics the functions of the HTCC and works in conjecture with it, providing particle identification instead at greater energies (>3GeV). Two panels within the FTOF identify particles using two-layer sets of scintillator bars with PMT readout channels. Particles can be recognized through their Pion/kaon/proton separation thresholds using two panels - 1a and 1b. Panel 1a covers $5^{o} < \theta < 35^{o}$ polar angle at a time resolution of 80ps, with additional coverage $>35^{o}$ at a lower 150ps resolution from panel 1b [19]. The Electromagnetic/Pre-shower calorimeters (ECAL/PCAL) are positioned at the frontmost end of the FD, they measure the energy of particles and assist with particle identification. Three tri-directional overlapping layers of scintillator bars separated by thin lead sheets create a readable surface of the calorimeters. A particle collision is measured by 3 sets of PMT readout channels, culminating in the layered signals creating a "pixel" on the surface. From this readout, a coordinate for a particle's "hit" can be calculated

Chapter 2.

Methodology

2.1 CLAS12 Software Framework

CLAS12 contains more than 100,000 readout channels from its combined subsystems, each outputting significant amounts of raw data information, which must be processed to identify the particles and reconstruct their path through the detector. This process can be separated into data acquisition and event reconstruction, Figure 2.11 shows this graphically. CLAS12's reconstruction and analysis processing framework (CLARA), is the overarching software that provides users with an easily scalable service-oriented architecture. Within this framework lies CLAS12's dedicated reconstruction software named the CLAS Offline Analysis Tools (COATJAVA). This structure provides users with common tools that make navigation and reconstruction more easily accessible. Additionally, it includes a series of software packages each with direct and specific functionalities for reconstruction.

- Talk about relevant software packages

2.1.1 Raw Data Acquisition

Initial raw data processing within CLAS12 goes through three stages to be processed into a format the software can analyse. Firstly, the time-to-digital converters (TDCs) and analogue-to-digital converters (ADCs) process signals into a digital form. This form easily and efficiently stores data into information such as signal strength, position, and time in the calorimeters and FTOF, or the number of photoelectrons in the Cherenkov counters [21].

2.1.2 Event Reconstruction Process

A three-stage Trigger system is used for data collection and is the preliminary action taken for reconstruction. An initial Global Trigger maps particle locations and trajectories through Geant4 simulations of CLAS12's geometry, topology, and readout channels. The first stage collects the ADC information, performing reconstruction based on hits and clusters generated by each subsystem's software algorithm. Stage 2 uses information from the TDCs to match coincidence clusters, timing, and geometry between detectors, and subsystems. The final stage collects the previous trigger bits into a single stream to be sent to the Data-acquisition-system (DAQ) [22]. Raw data collected by the DAQ is stored in the collaboration's Event Input/Output (EVIO) data format and compressed into a dedicated high-performance output (HIPO) file type. This file type has special indexing features, allowing the files to be easily differentiated based on the event particle information. Banks store and sort this data to then be processed by dedicated

algorithms within each detector subsystem. Firstly, hit-based tracking (HBT) is performed: where tracks are reconstructed based on hit positions on each subsystem, and information such as particle timing, momentum, and energy is matched to the track. This is sent through the event builder (EB), which sorts this information into Reconstruction (REC) banks based on which process it was generated by, as shown in Figure 2.11. Finally, time-based tracking (TBT) is performed: where the REC banks are sent back through the EB and are given an event "start time" [21], which assists with calibrating more accurate tracks and timing information through the reconstruction process. Additionally, the EB functions as a generalized particle identifier: allocating and storing information such as three momentum (px, py, pz) and energy deposited under particle IDs (PIDs) for each particle in an event.

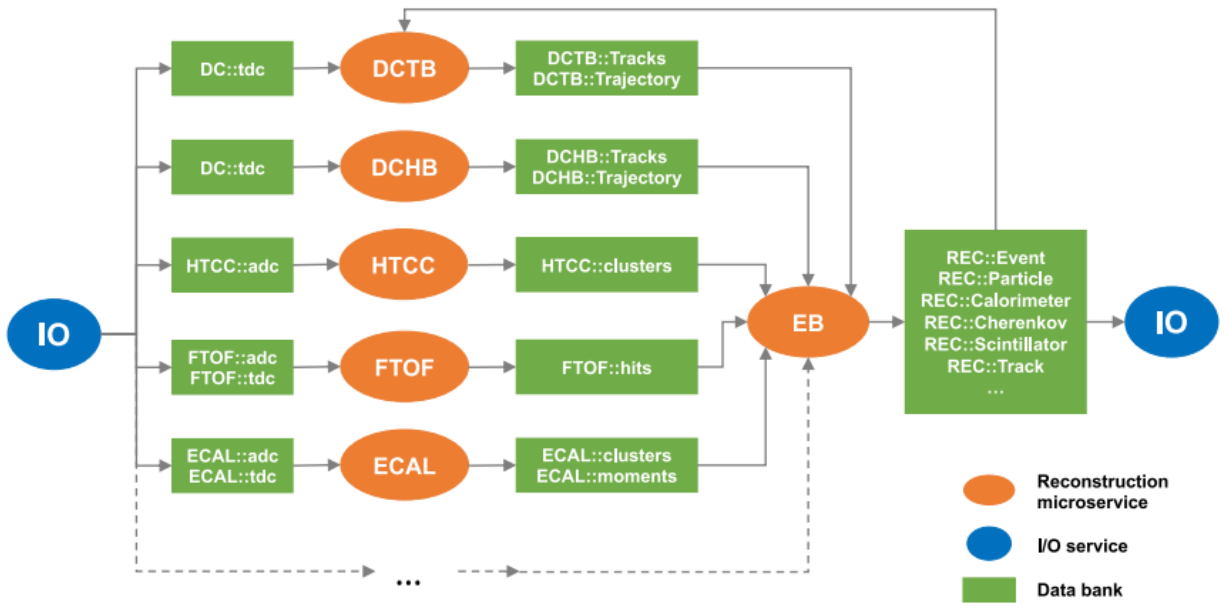

Figure 2.11: Graphical representation of the reconstruction process, showing processing of data from the Input/output package, through databanks, software packages and finally through the event builder into relevant reconstruction banks and output files.

2.1.3 Additional Cuts

Throughout reconstruction, certain are applied to particles through each subsystem within CLAS12 for optimal data selection, these cuts are taken from [23]. Electron vertex cuts on the target ensure electrons that scatter outside the target window are discarded. Photoelectron cuts select any photoproductions within the HTCC and LTCC that produce more than 2 photoelectrons. Fiducial cuts on the Calorimeters ensure hits are within either 9cm, 14cm or 19cm of the edge of each sector. The Drift Chambers also follow this sector edge cut, with the cut being made on the chi-squared (χ^2) distribution through the tracks.

2.2 Neutron Detection Efficiency

Neutrons produced pass through CLAS12 undetected as they cannot be tracked by the majority of the components in the CD and FD. These Neutrons are only fully recognized upon reaching the calorimeters (ECAL/PCAL) at the forward end of the detector. Neutrons are detected through reconstruction of the particle shower created upon a neutral collision with the PCAL, and after applying cuts and selection criteria. This study shows that CLAS12 detects and recognizes neutrons at less than 100% efficiency and that this Neutron Detection Efficiency (NDE) must be further investigated. The NDE is calculated from the ratio of expected over-detected neutron hits, given by equation 1.41:

$$NDE = \frac{H(e, e'\pi^+ n)}{H(e, e'\pi^+)n} \quad (1)$$

2.2.1 Event Selection

The Event Builder provides a "train" process [21] that translates particle information into a final output format named data summary tapes (DST). This train is a shortcut for physics analysis as it applies filters to recognize different final states in the detector. The reaction chosen to determine the NDE is: $e^- + p \rightarrow e' + \pi^+ + n$, this is labelled the final state e'π^+n, as seen in equation 1.41. This event choice assumes an electron colliding with a hydrogen target, producing a scattered electron, positive pion, and neutron. This reaction suggests that these particles are the only possible products, and the only neutral hit must be a neutron (discarding any possible photons as neutral hits). This process works internally by iterating over all events in a dataset, selecting only events with the PIDs for these particles, and discarding any events otherwise.

2.2.2 NDE Method

Information on particle positions and momenta provided by the detector's event reconstruction process allows for the charged products to be "swum" from the hit coordinate back to the locate at which the target was struck (the electron target vertex). As the charged particle momenta is known, a missing momentum bin for the neutron is calculated. Using this information, a virtual neutron track is swum and extrapolated from the target vertex, and the coordinates of the hit on the calorimeter are measured. The hit location is labelled an "expected" neutron, and denoted by H(e,e'π^+n). Neutral hits measured on the surface are labelled as "detected" neutrons, denoted by H(e,e'π^+)n.

2.2.3 Difference in Direction Cosine

To extract both the expected and detected neutron hits on the calorimeter, a difference in direction cosine cut is applied, as shown in Figure 3.21. The coordinates are such that the z-frame is the direction of the expected track, so the cut applies the transverse x and y momentum for each neutral. The Momentum in x and y of detected neutrals within a region around the expected hit are recorded as detected neutrons A cut is applied around the central region calculated from $\sqrt{\Delta C_x^2 + \Delta C_y^2}$, and controlled by the parameters in Table 2.22. The detected neutron with the smallest value from this cut is selected, discarding all other hits, this process is repeated fo r each event

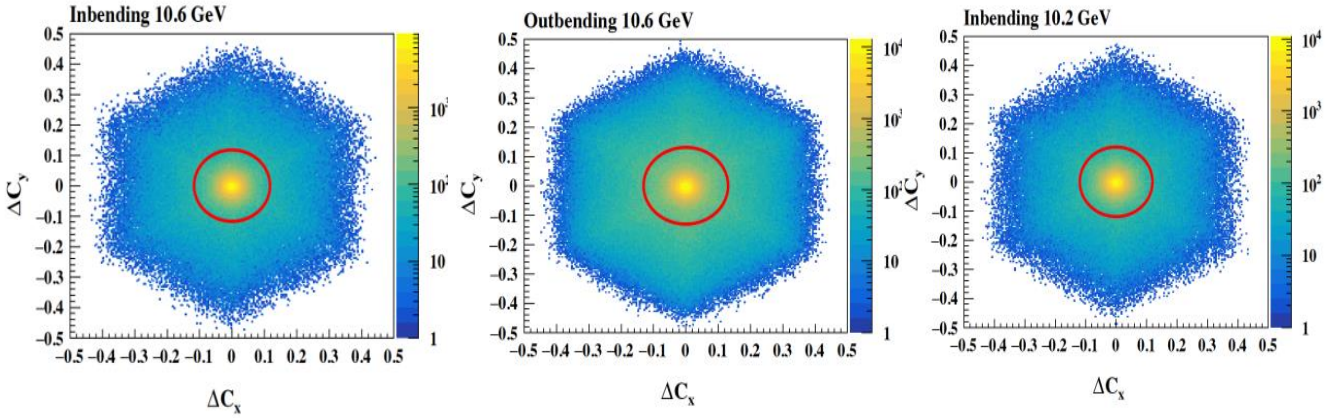

Figure 1.41: Difference in direction cosine from the electron vertex, showing the total yield of all combined events. All three datasets used are shown. The red circle is the cut applied to eliminate significant background noise. Taken from [22].

Cut Applied	Dataset
<0.1174 (11.74%)	Inbending 10.6GeV
<0.1308 (13.08%)	Outbending 10.6GeV
<0.1195 (11.95%)	Inbending 10.2GeV

Table 2.21: Providing information on applied cuts for the $\sqrt{\Delta C_x^2 + \Delta C_y^2}$ calculation. Each of the three datasets shown uses a slightly different cut. From [22].

2.3 Neutron Missing Mass Spectra

The e'π^+n reaction used for measuring the NDE is sorted into many separate histograms in the HIPO file format, which can be obtained and viewed through a CERN-developed framework called ROOT. The applicable histograms for this study place the neutron signal over its Missing Mass (MM), producing a missing mass spectrum. The Expected and Detected neutron signals are extracted from the same dataset and hence the same parent histogram. As Energy increases at CLAS12. the spectrum contains more background noise beyond and within the MM peak centralized around the neutron massing mass (0.9354MeV).

2.3.1 Alternate Datasets

- Talk about all 3 datasets here and how important they are
- CB only has in bending 10.6 as at the time of fitting it was the only dataset with appropriate magnetic corrections applied

2.3.2 Missing Momentum

Due to the large kinematical range and large background noise produced at CLAS12, the missing mass spectra are separated into separate Missing Momentum bins spread from 0.375-7.5GeV. The Data does not reach the maximum 10.2-10.6 GeV (depending on the dataset used from Table 2.21) due to the background being indistinguishable from the neutron signal at higher energies (See Appendix C.1/C.2 for

validation). We use 36 Missing Momentum bins sorted for CLAS12, each with a varying range of momenta and producing MM spectra that can be individually fitted.

2.3.3 Extracting the Neutron Signal

The goal of fitting these spectra is to extract the Neutron signal separate from the background signal intruding upon the missing mass, this is to eliminate any noise and ensure the only products within the yield are neutrons. To do this we fit a function to the MM histograms and measure the total neutron yield this function produces. We apply a Definite integral within a user-defined range over the function and measure the background signal independently from the neutron signal peak. By fitting the background as a separate polynomial from the function, we can summate them and produce separate signals that can be extrapolated and subtracted. Expected and Detected fits are performed

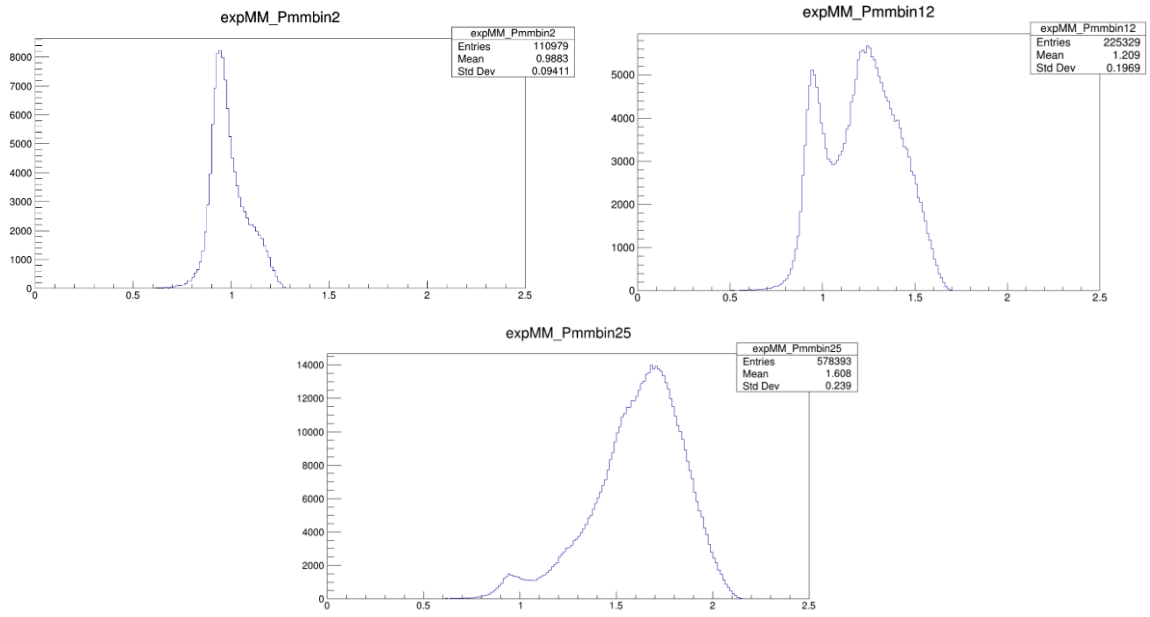

Figure 2.31: Missing Momentum bins 2, 12, and 25, taken from the raw ROOT file of Inbending 10.6GeV data, these histograms are used in the function fitting in the upcoming sections.

separately from one another and are analysed separately to obtain individual yields. We can then compare the expected and detected yields from equation 1.41 to determine the NDE across the missing momentum distribution.

2.4 Histogram Fitting Procedures

The Core of a Missing Mass spectrum follows the characteristic symmetric "bell-curve" shape of a normal distribution. From this judgment, fitting with a Gaussian or a Gaussian-like function is appropriate. Currently, the NDE has been fitted with a Gaussian Function and a Crystal Ball function. This study investigates the comparable differences between these functions and a Double Crystal Ball Function (see sections 2.4.1, 2.4.2, 2.4.3). From Figure 2.31, it is expected that the parameters of a fitted function should vary smoothly and increase with missing momentum, as we see the signal shift right, and the background increases.

2.4.1 Higher order Polynomial Background

All fits are done with a fourth-order polynomial background as this provides the minimum number of turns needed. Higher-order polynomials are also suitable for fitting, as they provide adequate turns, however, too many turns raise the number of degrees of freedom and can lead to poor results, see section []]]]]]. The Gaussian Parameters must be obtained before proceeding with more complex functions as they are the purest form of these parameters before additional terms are introduced.

2.4.2 The Reduced Chi-Squared

When fitting to histograms, the suitability of the fit depends on the Reduced Chi-squared statistic, measured as chi-square (χ^2) per degree of freedom ν.

$$\chi^2_\nu = \frac{\chi^2}{\nu} \quad where\ \chi^2 = \sum_i \frac{(N_i - C_i}{\sigma_i^2}\ ,\ \nu = n - m \quad (2.41)$$

$$where\ \chi^2 = \sum_i \frac{(N_i - C_i)}{\sigma_i^2}\ , \quad \nu = n - m \quad (2.42)$$

Where N is the fit observation, C is the calculated data, σ^2 is the variance, n is the number of observations and m is the number of fitted parameters. The consistent goal when fitting is to retain the lowest possible reduced chi-square value, as this proves the "goodness" of the fit. If the reduced chi-square is abnormally large, this suggests the fit has failed somewhere, or is inaccurate at some point within the fit range

2.4.3 Starting Point - Gaussian Function

A parametrically extended Gaussian is the purest fitting procedure possible for extracting the yield as the only variable parameters are the mean (μ), width (σ), and amplitude. It is used as no additional systematic uncertainty arises from increasing the function's complexity with additional terms. The procedure for fitting a Gaussian is as follows:

- Begin with a reasonable starting point for the mean and width parameters, the most appropriate being the Neutron missing mass (0.9395MeV). This can either be from prior understanding or an initial fit.
- Fit the lowest missing momentum detected neutron bin first, this is for two reasons: the detected bins will be the most accurate to the real neutron hit on the calorimeter. The lowest missing momentum contains the least background intrusion, and therefore, the purest fit.
- Fit each subsequent detected bin using the previous bin's parameters generated as the starting point for the current bin's parameters, providing reasonable limits. At this point, it is appropriate to provide very wide limits as this gives the fitting procedure the most time to find the correct parameters.

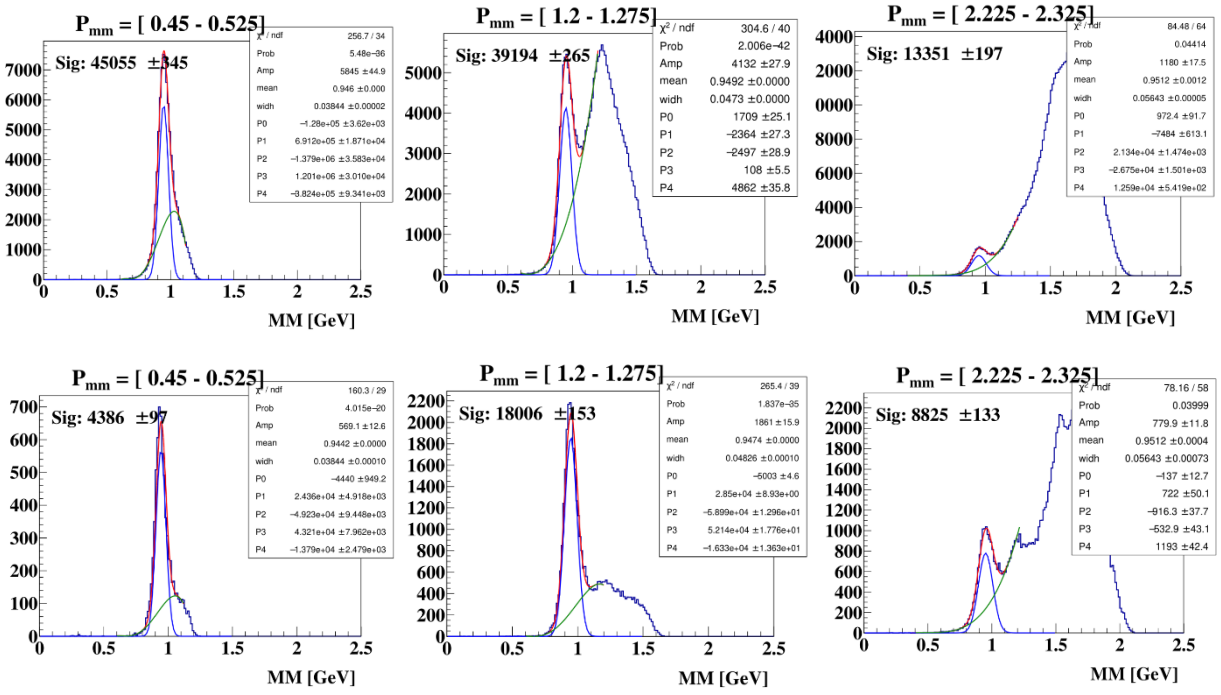

Figure 2.41: Plots at three different missing momenta of fitting the NDE data using a Gaussian Function, the top row is expected, and the bottom row is detected. The blue line is the Gaussian, the green line is the polynomial background, and the red line is the sum of the two.

- Reproduce the same steps for fitting for each expected bin, except use the values of the completed 36 detected bins as the parameters for each bin.
- Look for the reduced chi-squared (χ^2), and adjust the parameters mean (μ), width (σ), and amplitude until the lowest value for the χ^2 between the expected and detected bins is produced.

2.4.2 Gaussian Parameter Shift

Figure 2.41 shows 3 expected and 3 detected bins performed using a Gaussian Function and fourth-order polynomial background. They consistently fit the histograms in Figure 2.31, however, it becomes apparent that the mean should shift to higher missing mass as missing momentum increases. The parameters mean (μ), width (σ), and amplitude vary smoothly, where the mean lies within 0.94-0.96MeV and the width lies within one standard deviation. However, with increasing missing momentum, the mean was observed to gradually increase away from the neutron missing mass (0.9395MeV) and the width increased to greater than one standard deviation. This observed variation is caused by minute errors in the drift chamber's (DCs) magnetic field mapping, these errors have been corrected by adjusting the electron and pion momentum information accordingly. Due to the low systematic uncertainty of the Gaussian fit, its parameters are used as the starting points for the fitting of any Gaussian-like functions, so the Parameterization shown on the plots in Figure 2.42 must be optimal.

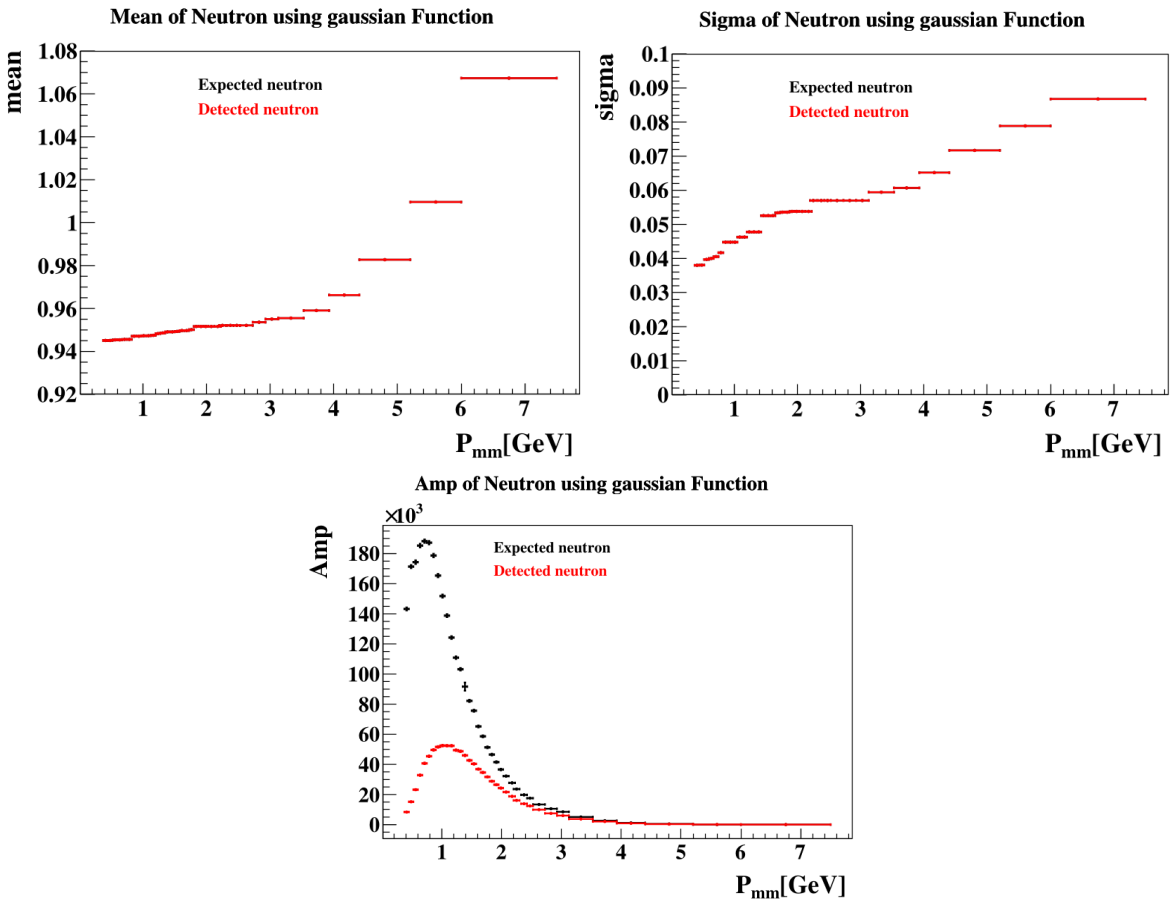

Figure 2.42: Parameters mean (μ), width (σ), and amplitude plotted after fitting with a Gaussian function and fourth-order polynomial background. Showing smooth variation of parameters and the mean/width shift. Ranges are fixed hence there are no error bars present.

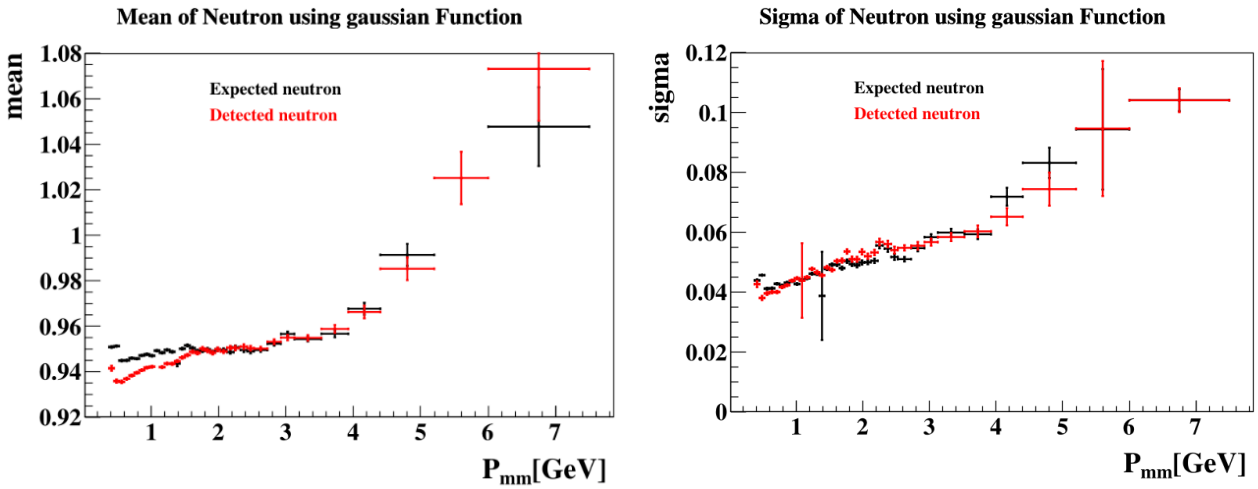

Figure 2.43: Parameters mean (μ), and width (σ) plotted after fitting with the same conditions as Figure 2.42, making parameter range loose to reveal expected and detected independent parameter shift.

The comparable background yield from neutron yield in the expected fits in Figure 2.41 is noticeably larger at the same missing momentum than the detected bins, suggesting the mean shift altered slightly for the expected bins. This is observed in Figure 2.43, where the parameter range has been allowed to vary largely, causing the expected and detected Gaussian parameters to differ by up to 3%. This difference alone causes the NDE ratio results in section 2.2 to be poor. This is shown by Figure 2.44, where the originally smooth NDE becomes inconsistent.

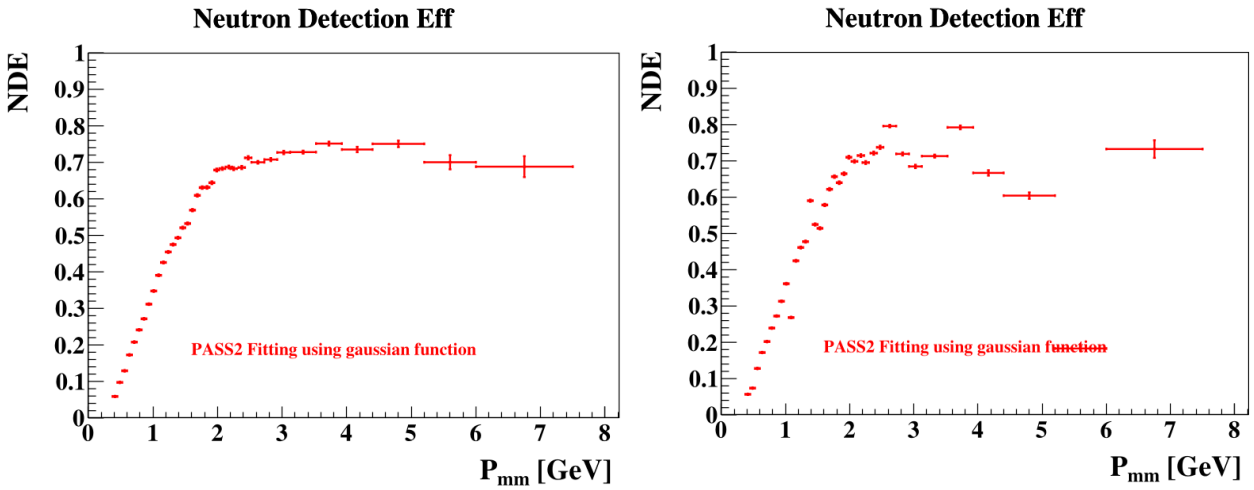

Figure 2.44: NDE ratio plotted after fitting using a Gaussian with fourth order polynomial. (left) NDE using fixed Gaussian parameters (Figure 2.42), (right) NDE using loose parameters (Figure 2.43), showing poor fit.

2.4.3 Crystal Ball Function

The Crystal Ball Function—named after the Crystal Ball Collaboration—was formulated in 1979 by the Stanford Linear Accelerator Facility (SLAC) group as a viable function to model lossy effects in high-energy particle physics. It consists of a Gaussian core component with a power-law tail stitched onto either side, at low or high missing mass, this is user-defined.

$$f(x: \bar{x}, \sigma, \alpha, n) = N \begin{cases} \exp\left(\frac{(x-\bar{x})^2}{2\sigma^2}\right), & for\ \frac{x-\bar{x}}{\sigma} > -\alpha \\ A\left(B - \frac{x-\bar{x}}{\sigma}\right)^{-n}, & for\ \frac{x-\bar{x}}{\sigma} < -\alpha \end{cases} \quad (2.43)$$

$$A = \left(\frac{n}{|\alpha|}\right)^n exp\left(-\frac{|\alpha|^2}{2}\right) \quad (2.44)$$

$$B = \frac{n}{|\alpha|} - |\alpha| \quad (2.45)$$

This functional form determines whether to fit a Gaussian component (top) or power-law component (bottom), depending on the location of the tail parameters. Parameter α determines the point at which the tail attaches to the Gaussian core, measured in standard deviations from the mean, parameter n is the amplitude of the tail. Giving the parameter α a negative value places the tail at high MM and using a positive α value places the tail at low MM. This function is then multiplied by some normalization factor N; this is typically a corrective value to account for the amplitude of the fit. Figure 2.41 shows An oversimplified Crystal Ball Function that is plotted with varying tail parameters to show their effects.

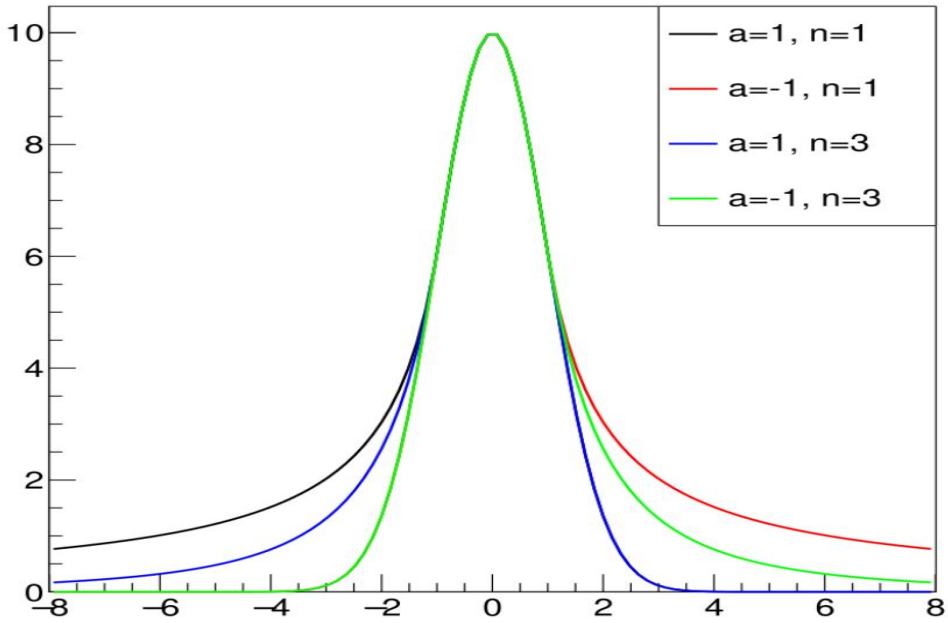

Figure 2.41: Simple Crystal Ball Function Plotted with 4 different sets of arbitrary parameters shown in the legend, each with a corresponding color.

2.4.4 Double Crystal Ball Function

The Double Crystal Ball Function is similar, with the addition of another MM tail on the other side of the Gaussian core. Equation 2.42 shows that it is mathematically identical to the Crystal Ball function, with variability from two additional tail parameters α_L, and n_L, which provide the function with two additional conditions. Due to this, the Double Crystal Ball Function requires further parameterization of the i^{th} tail for constants A and B and the overall fit. This function can be in Symmetric or Asymmetric form. It is predicted that the symmetric function should have a lower chi-squared (χ^2) due to having more degrees of freedom.

$$f(x:\bar{x},\sigma,\alpha,n) = N\begin{cases} \exp\left(\frac{(x-\bar{x})^2}{2\sigma_R^2}\right), & for\ \frac{x-\bar{x}}{\sigma} \le \alpha_R \\ \exp\left(\frac{(x-\bar{x})^2}{2\sigma_L^2}\right), & for\ \frac{x-\bar{x}}{\sigma} \le 0 \\ A_L\left(B_L - \frac{x-\bar{x}}{\sigma}\right)^{-n_L}, & for\ \frac{x-\bar{x}}{\sigma_L} < -\alpha_L \\ A_R\left(B_R + \frac{x-\bar{x}}{\sigma}\right)^{-n_R}, & otherwise \end{cases} \quad (2.42)$$

$$A_i = \left(\frac{n_i}{|\alpha_i|}\right)^{n_i} exp\left(-\frac{|\alpha_i|^2}{2}\right) \quad (2.42)$$

$$B_i = \frac{n_i}{|\alpha_i|} - |\alpha_i| \quad (2.43)$$

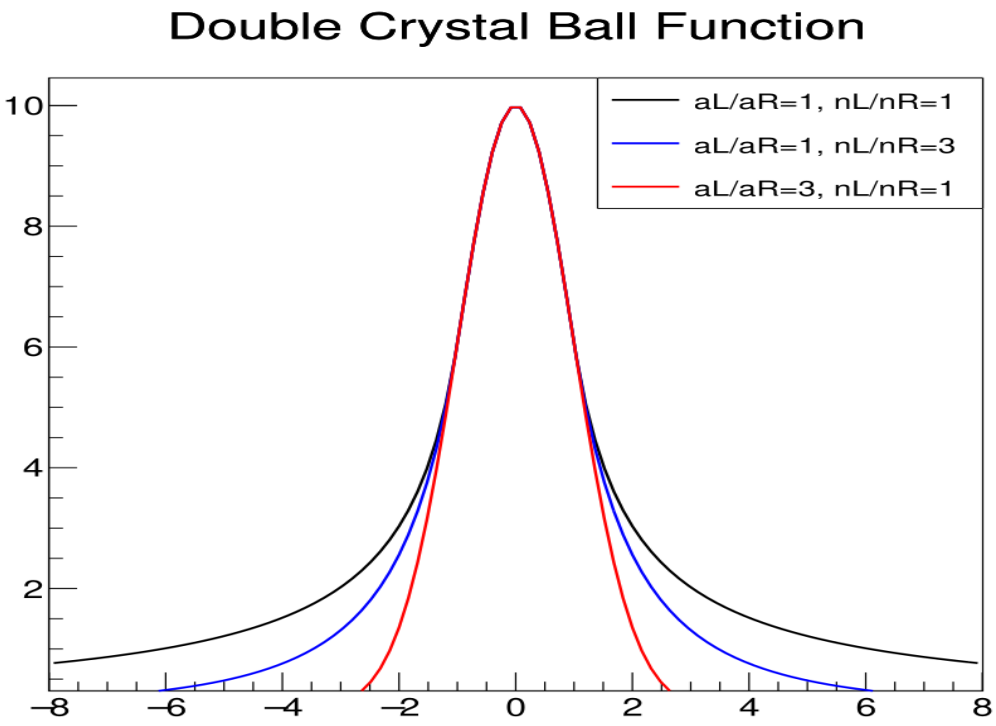

Figure 2.42: Simple Symmetric Double Crystal Ball Function Plotted with 3 sets of arbitrary parameters shown in the legend, each with a corresponding color. Shows how the parameters αL/αR and nL/nR affect the fit shape.

2.5 Double Crystal Ball Fitting Procedure

We use the same histograms to fit the MM data, so fitting with a double crystal ball function begins with fitting the Gaussian function in section 2.4.2. We retain the Gaussian parameters and keep them fixed for the Double Crystal Ball fitting procedure, except the amplitude can vary as the tails may alter this slightly. The tail parameters α_L, α_R n_L, and n_R are the additional terms we must account for.

2.5.3 Power-law Tail Parameterization

Similarly to the Gaussian parameters, from Figure 2.31, we expect the tail terms to vary smoothly as missing momentum increases as they are attached to the Gaussian core. Due to this, the fitting procedure is similar and is as follows:

- Begin with reasonable tail values for the first detected bin, these can be assumed from your detected Gaussian parameters mean (μ), and width (σ). Provide them with a loose range, allowing ROOT to find suitable parameters.
- Use the previous bin's tail parameters as starting points for the upcoming detected bin, repeat this for each bin.
- Use the 36 detected bin parameter values as starting points for each parameter in the expected bins, repeating the previous step.
- Reiterate as necessary to produce the lowest reduced chi-square value possible for both expected and detected fits.

2.5.4 Alternative Fitting Procedures

In Sections 2.4.2 and 2.4.3, the procedure for fitting the Crystal Ball and Double Crystal Ball Functions is shown, this method has been used consistently and is found to be the most appropriate. However, there are alternative ways to perform this fitting which could be accounted for in future applications: forced iterative fitting and Preparatory background fitting. Force iterative fitting makes use of Python looping functionalities, where you provide the fit with an array of 36 percentage ranges and iterate over the full 36 bins. I found this method to be suitable for automating the fitting process, as although it takes significant time, ROOT eventually finds the most appropriate parameters, this is explored more in section []]]]. Preparatory background fitting is performed by fitting the polynomial background within its appropriate range before fitting any functions in the signal region, this can provide the user with a pure background fit before any effect from fitting functions, which can be more appropriate, see section []].

2.5.5 Fitting Goals (temporary)

- Comparing Gaussian parameters between fits
- Comparing influence of additional parameters / tails / functions on signal yield, NDE, and the parameters between functions (CB and DCB)
- Find the most optimal function (and background) for extracting the NDE

Chapter 3.

Validation and Results

3.1 Double Crystal Ball Fitting Results

Fitting, and comparing the Double Crystal Ball Function to previously accomplished NDE fits is the main goal of this study, and in the upcoming sections, these results of the fitting are discussed in detail.

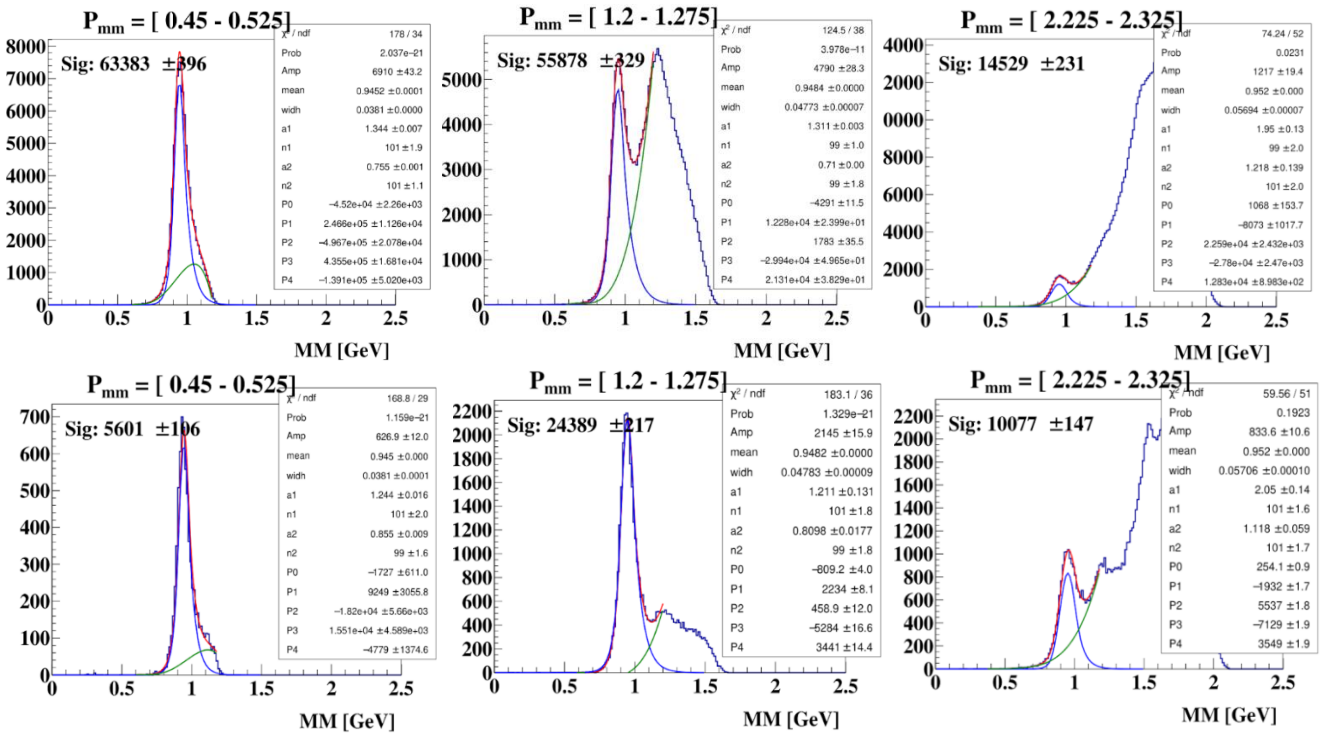

Figure 3.11: Missing Mass fits for a Double Crystal Ball Function with a fourth-order polynomial background. The Missing momentum bins have the same properties as Figure 2.41.

3.1.1 Tail Parameter Trends

As Missing Momentum increases, the tail parameters shift, similarly to the Gaussian Parameters. We expect this as the tails are dependent on the location and shape of the Gaussian, from equation 2.42. Additionally, the Gaussian parameter shift (see section 2.4.2) indicates the tail parameters should also shift by a similar degree, increasing gradually with missing momentum.

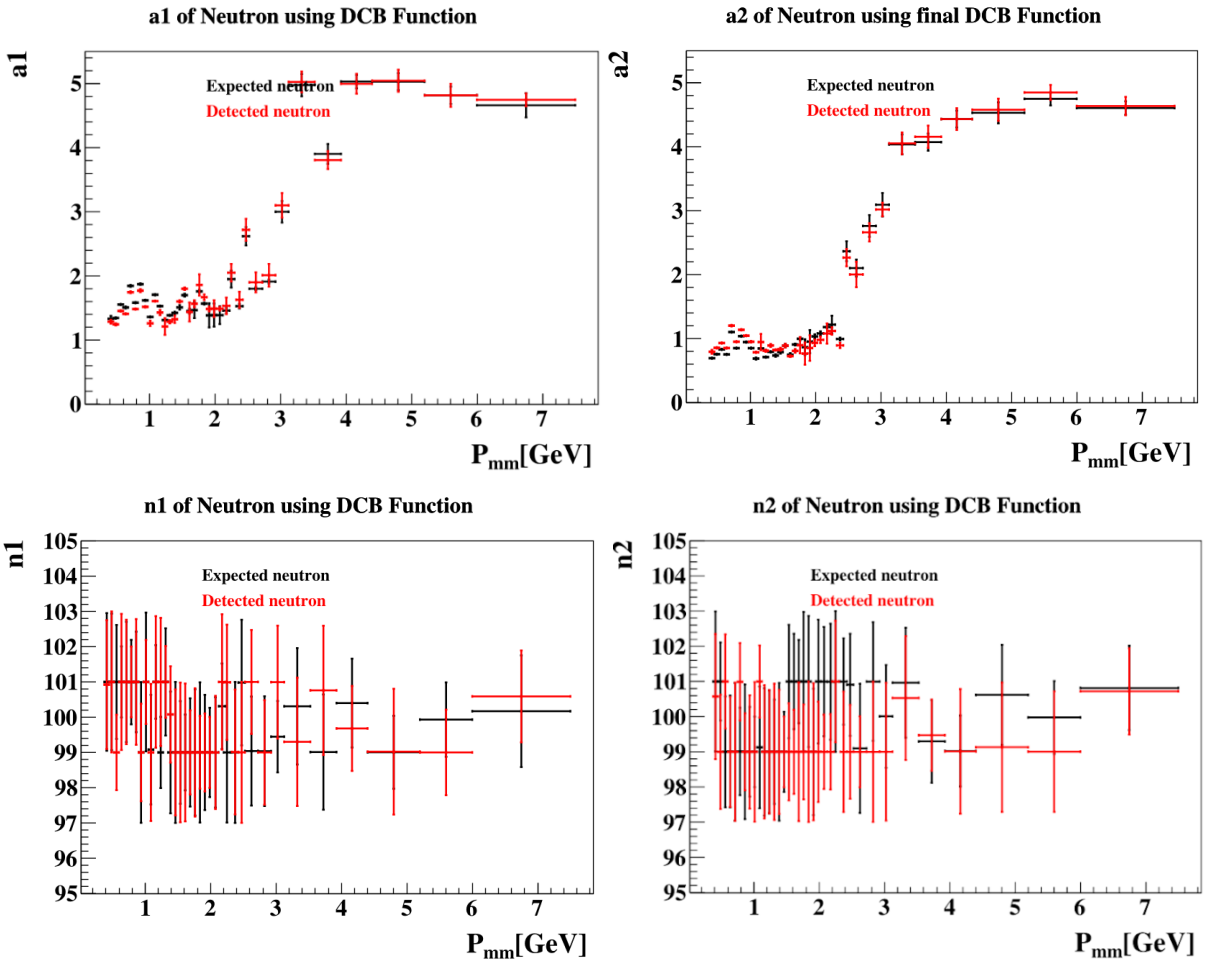

Figure 3.12: Tail Parameters aL, aR (top), and nL, nR (bottom) plotted as a function of missing momentum Pmm, the red points are detected neutrons, and the black points are expected neutrons.

Parameters a_L, and a_R, vary gradually over the missing momentum range as we expect, however, they prove to be sporadic and unstable, where their positions are inconsistent, and ROOT struggles to find the most appropriate location to place them. The parameters n_L, and n_R, however, is kept consistent for all fits when determining the best chi-square, remaining at ~100, and not being varied. ROOT also does not object to these values and changing them has little effect on the fitting procedure. It is important to note that, unlike the Gaussian Parameters, it is appropriate to have different tail parameter values between the expected and detected fits (see section 3.1.3)

3.1.2 Symmetry and Asymmetry

A Double Crystal Ball function has functional symmetry and asymmetry, which is dependent on the tail parameters chosen. Symmetry – tails determined by a_L, a_R, and n_L, n_R will be the same size on either side of the mean (n_L, n_R will be the same). Asymmetry – the tails will be different sizes on either side of the mean (n_L, n_R can be different). However, a_L, a_R can be different or the same for both of these cases, the values of which affect the chi-square significantly. It is expected that symmetric fits should have a lower reduced chi-square, as from equations 2.41/2.42 there are more degrees of freedom, this is discussed in section 3.1.3.

3.1.3 Reduced Chi-squared Results and Dependence

Similarly to the Gaussian Parameters, the tail parameters marginally affect the reduced chi-square of our fit based on their final values. They have a specific range where they are appropriate and placing them outside of this range can instead cause a large variation in the chi-square or cause the fitting procedure to error.

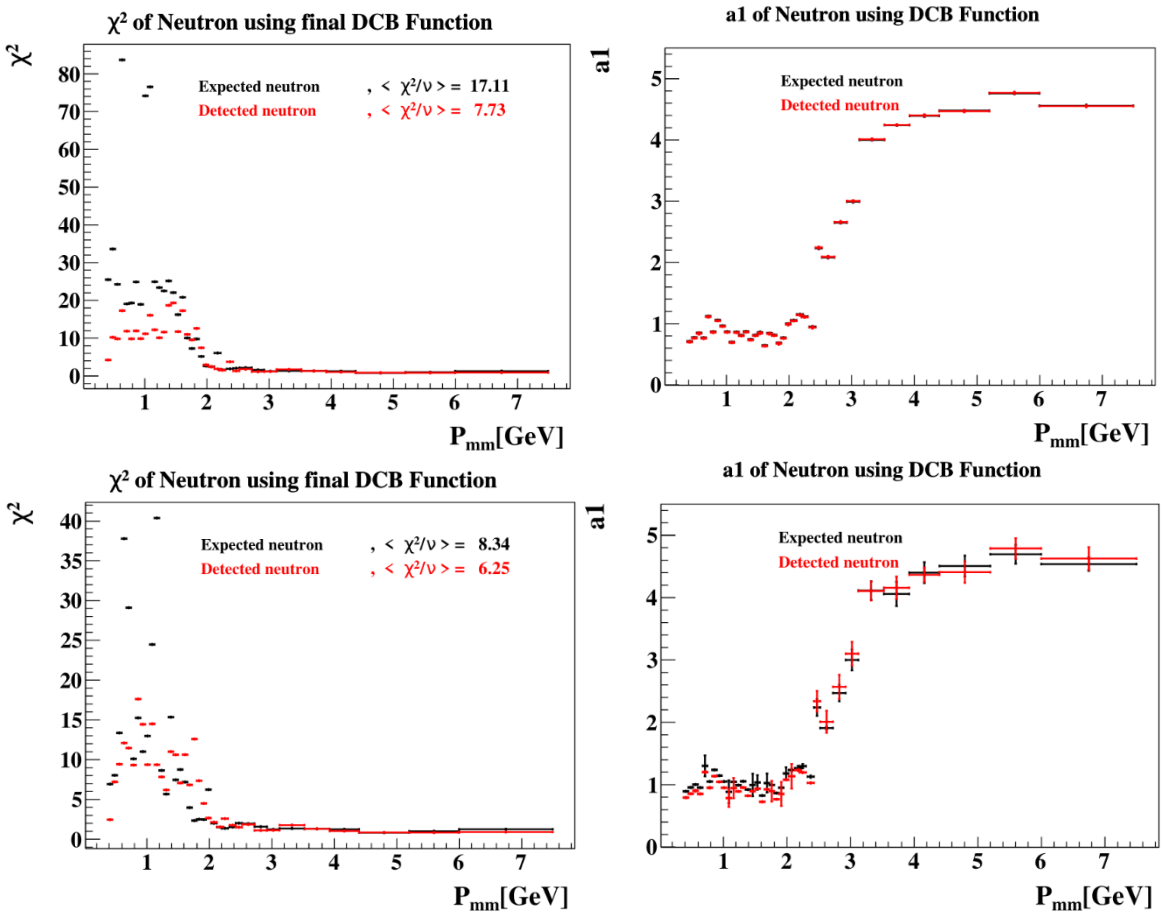

Figure 3.13: Reduced chi-square (left) shown to vary based on the position of parameters aL and aR (right). Top plots show the effect when tail parameter aL is made to equal aR, where expected and detected points are kept equal, bottom plots show the effect when the parameter position aL is made to equal aR alone.

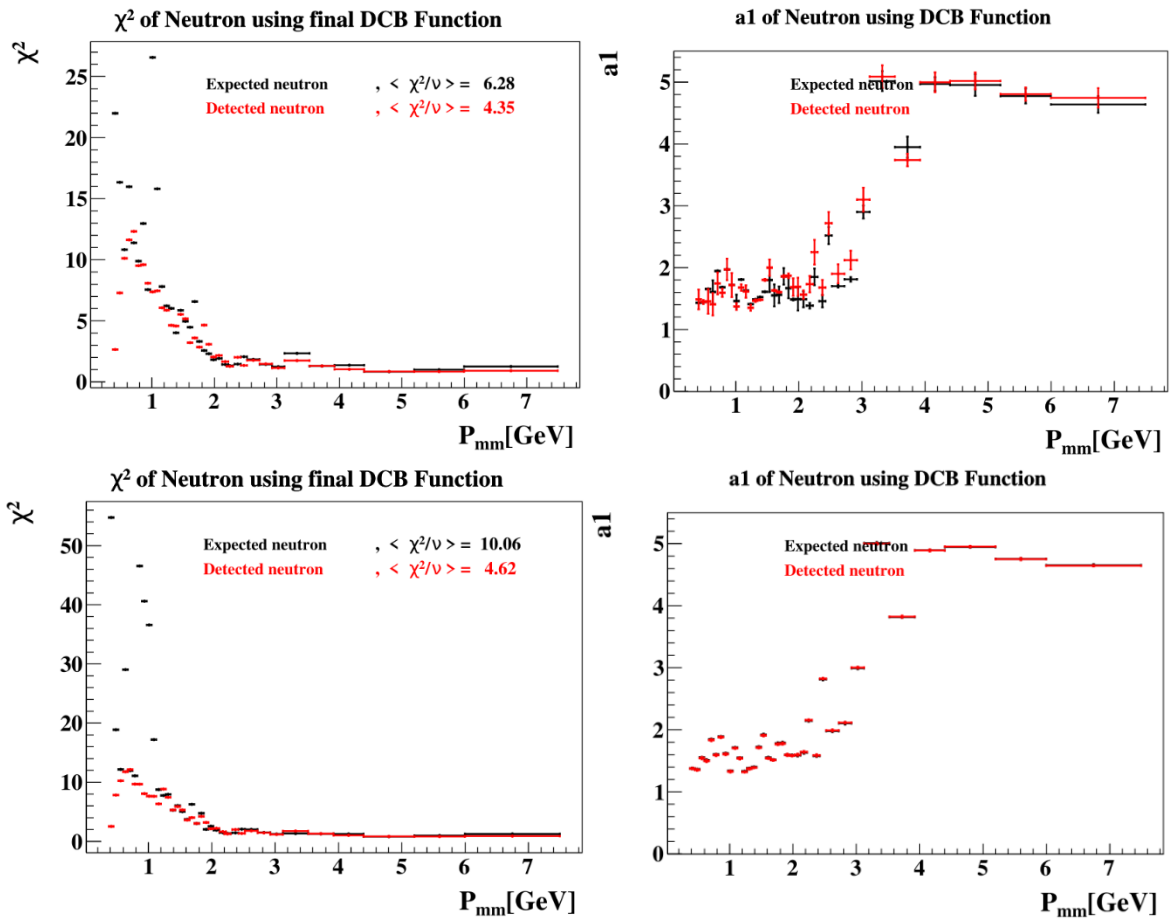

Figure 3.14: Reduced chi-square (left) shown to vary based on the position of parameters aL and aR (right). Top plots show the effect when tail parameter AR is made to equal aL, where expected and detected points are kept equal, bottom plots show the effect when the parameter positions AR is made to equal aL alone.

The reduced chi-square consistently increases from its optimal value in all of the above cases, where both tail position and expected/detected points cause an effect. However, the increase is more significant and more apparent when forcing the parameters to have the same expected and detected points. This is due to this change forcing the parameters away from their optimal values, reducing the fit quality, so it is imperative to adjust the tail parameters to have the most accurate values.

[FINISH THIS SECTION BY TALKING ABOUT GENERAL CHI-SQUARE RESULTS]

3.1.4 Universal Signal Increase

Figure 3.15 shows the total signal produced by each fitting method. The total signal changes by a predictable amount as you would assume each tail captures more yield within the definite integral. The Crystal Ball shows ~5% more yield than the Gaussian and the Double Crystal Ball shows ~23% more yield than the Gaussian. The Increase differs between the two, showing that the low MM tail captures less background than the high MM tail that is introduced from the Double Crystal Ball Function. This is very consistent for low missing momentum, but the difference consistently loses effect as missing momentum increases. We can imply that the tails are very prevalent at low missing momentum but negligible at higher missing momentum.

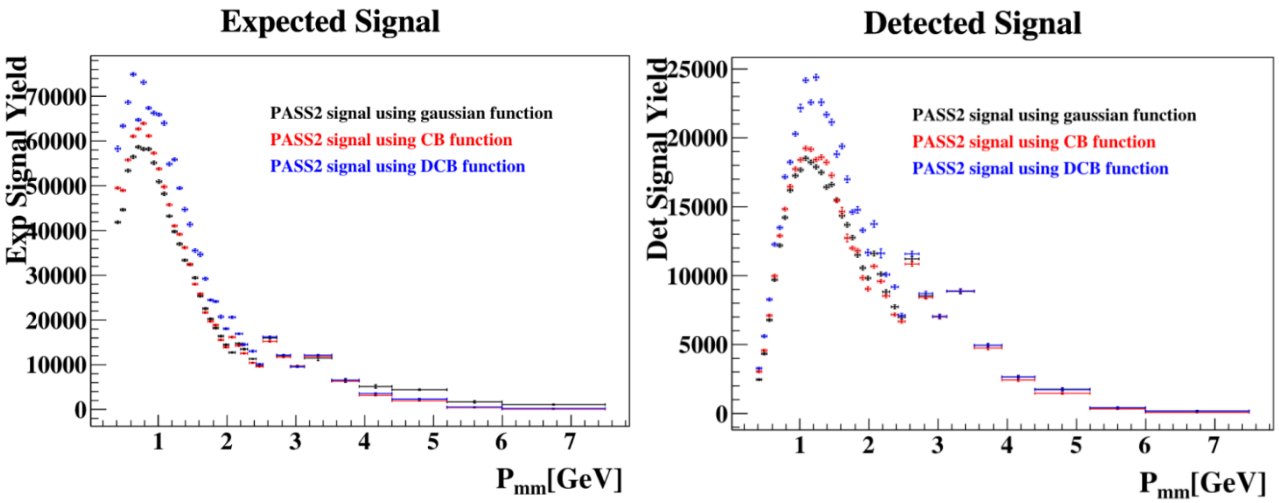

Figure 3.15: Plots showing the signal extracted from the background, produced by the definite integral between the ranges given in figure [][][][][. Shows that the DCB and CB tails introduce more signal to the NDE ratio.

3.1.5 Higher and Different Order Polynomials

It is well understood that fitting with a fourth order polynomial background best represents the background signal in the missing mass spectrum, and it is th

- Discuss how 3rd order is possible but expected bin is strangely off
- Discuss how 5th order works just as well as 4th order
- Prediction that any order higher than 4th should work based on these results

3.1.6 NDE results

- Plots of NDE comparison go here
- Plots of difference between two go here, talk about appropriate limits

3.1.7 Forced Iterative Fitting

- This method is great for getting lowest chi square possible and great for getting best MM spectrum fits
- Takes a long time and require some solid basic assumptions
- Only real change is in the chi-square, which is expected as the expected/detected bins reach their individual most accurate points
- Not acceptable with the current method to use for the NDE due to this

3.1.8 Preparatory Background Fitting

- This fits the background a lot better than when fitting it with the function simultaneously
- Although the polynomial terms vary significantly from original
- This means when extrapolating back into DCB function they just return to their original values
- Additionally when fixing them to the good values from the background fitting, the fits fail as the range is updated and the polynomial is now inappropriate for that new range.
- Should test further by limiting ranges on new fits more..... WORK STUFF

Chapter 5.

Discussion and Conclusion

Chapter 6.

Bibliography

[1] Robinson, A.L. (1980). A Long-Range Plan for Nuclear Science. *Science*, 210(4475), pp.1236–1237. doi:https://doi.org/10.1126/science.210.4475.1236

[2] Bodi, A., Bálint Sztáray, Baer, T., Johnson, M. and Gerber, T. (2007). Data acquisition schemes for continuous two-particle time-of-flight coincidence experiments. *Review of scientific instruments online/Review of scientific instruments*, 78(8). doi:https://doi.org/10.1063/1.2776012.

[3] Whitlow, L.W., Riordan, E.M., Dasu, S., Rock, S. and Bodek, A. (1992). Precise measurements of the proton and deuteron structure functions from a global analysis of the SLAC deep inelastic electron scattering cross sections. *Physics Letters B*, 282(3-4), pp.475–482. doi:https://doi.org/10.1016/0370-2693(92)90672-q.

[4] Marciano, W. and Pagels, H. (1978). Quantum chromodynamics. *Physics Reports*, [online] 36(3), pp.137–276. doi:https://doi.org/10.1016/0370-1573(78)90208-9.

[5] Banerjee, B., Glendenning, N.K. and Matsui, T. (1983). Meson radiation from a quark-gluon plasma by fission of chromoelectric flux tubes. *Physics Letters B*, 127(6), pp.453–457. doi:https://doi.org/10.1016/0370-2693(83)90292-7.

[6] CONCEPTUAL DESIGN REPORT BASIC EXPERIMENTAL EQUIPMENT ELECTRON BEAM ACCELERATOR FACILITY RECEIVED. (1990). Available at: https://digital.library.unt.edu/ark:/67531/metadc674902/m2/1/high_res_d/491625.pdf [Accessed 12 Jun. 2024].

[7] Mecking, B.A., Adams, G., Ahmad, S., Anciant, E., Anghinolfi, M., Asavapibhop, B., Asryan, G., Audit, G., Auger, T., Avakian, H., Ball, J.P., Barbosa, F.J., Barrow, S., Battaglieri, M., Beard, K., Berman, B.L., Bianchi, N., Boiarinov, S., Bonneau, P. and Briscoe, W.J. (2003). The CEBAF large acceptance spectrometer (CLAS). *Nuclear Instruments and Methods in Physics Research Section A: Accelerators, Spectrometers, Detectors and Associated Equipment*, [online] 503(3), pp.513–553. doi:https://doi.org/10.1016/S0168-9002(03)01001-5.

[8] Youcai, Wang. (2010). Measurement of Single-spin Asymmetry in Charged Kaon Electroproduction on a Transversely Polarized ^3He Target.

[9] Sinclair, C., 1992. A 500kV photoemission electron gun for the CEBAF FEL. *Nuclear Instruments and Methods in Physics Research,* 318(1-3), pp. 410-414.

[10] Benesch, J.F. and Mammosser, J. (1995). CEBAF's SRF cavity manufacturing and some performance limitations. *IEEE Transactions on Appiled Superconductivity*, 5(2), pp.834–836. doi:https://doi.org/10.1109/77.402677.

[11] Reece, C. (2016). Continuous wave superconducting radio frequency electron linac for nuclear physics research. *Physical review accelerators and beams*, 19(12). doi:https://doi.org/10.1103/physrevaccelbeams.19.124801.

[12] Hovater, C., Arnold, G., Fugitt, J., Harwood, L., Kazimi, R., Lahti, G., J. Mammosser, Nelson, R., Piller, C. and Turlington, L. (1996). The CEBAF RF Separator System. *Prepared for*, pp.77–79. doi:https://doi.org/10.5170/cern-1996-007.77.

[13] Burkert, V. Et al. (2020). The CLAS12 Spectrometer at Jefferson Laboratory. *Nuclear Instruments and Methods in Physics Research Section A: Accelerators, Spectrometers, Detectors and Associated Equipment*, 959, pp.163419–163419. doi:https://doi.org/10.1016/j.nima.2020.163419.

[14] Stepanyan, S., Crede, V., Eugenio, P. and A. Ostrovidov (2010). Hadron Physics with CLAS12. *AIP conference proceedings*. doi:https://doi.org/10.1063/1.3483308.

[15] Luongo, C. Et al. (2016). The CLAS12 Torus Detector Magnet at Jefferson Laboratory. *IEEE transactions on applied superconductivity*, 26(4), pp.1–5. doi:https://doi.org/10.1109/tasc.2015.2510336.

[16] Y.G. Sharabian et al (2020). The CLAS12 high threshold Cherenkov counter. *Nuclear instruments and methods in physics research*. 968, pp.163824–163824. doi:https://doi.org/10.1016/j.nima.2020.163824.

[17] Mestayer, M.D et al (2020). The CLAS12 drift chamber system. *Nuclear instruments and methods in physics research*. 959, pp.163518–163518. doi:https://doi.org/10.1016/j.nima.2020.163518.

[18] David L. Price, F. F.-A., 2013. Neutron Scattering - Fundamentals. *Experimental Methods in the Physical Sciences,* Volume 48, pp. 1-506.

[19] Carman, D.S. Et al. (2020). The CLAS12 Forward Time-of-Flight system. *Nuclear instruments & methods in physics research. Section A, Accelerators, spectrometers, detectors and associated equipment*, 960, pp.163629–163629. doi:https://doi.org/10.1016/j.nima.2020.163629

[20] P. Chatagnon Et al. (2020). The CLAS12 Central Neutron Detector. *Nuclear instruments & methods in physics research. Section A, Accelerators, spectrometers, detectors and associated equipment*, 959, pp.163441–163441. doi:https://doi.org/10.1016/j.nima.2020.163441

[21] Ziegler, V. Et al. (2020). The CLAS12 software framework and event reconstruction. *Nuclear instruments & methods in physics research. Section A, Accelerators, spectrometers, detectors and associated equipment*, 959, pp.163472–163472. doi:https://doi.org/10.1016/j.nima.2020.163472.

[22] Baashen, L., 2023. *Neutron Magnetic Form Factory GMN Measurement at High Q squared with CLAS12,* Miami: Florida International University.

[23] CLAS Collaboration at Jefferson Laboratory. CLAS12 RG-A - Analysis Note Overview and Procedures, 2020. https://clas12-docdb.jlab. 141 org/DocDB/0009/000949/001/RGA_Analysis_Overview_and_ Procedures-08172020.pdf.

[24] B. Raydo. Et al. (2020). The CLAS12 Trigger System. *Nuclear instruments & methods in physics research. Section A, Accelerators, spectrometers, detectors and associated equipment*, 960, pp.163529–163529. doi:https://doi.org/10.1016/j.nima.2020.163529.

Chapter 7.

Appendices

Appendix A: Literature Review

Literature Review: Neutron Detection Efficiency of the Jefferson Lab CLAS12 Detector

Jude Buckley 6692283

July 2024

Abstract

This paper is an overview of the Jefferson lab and its history, from the NSAC long-range report in 1979, to it's completed construction in 1995 as a facility that uses new accelerator and detector technology, and pioneer research into quantum chromodynamics and quark structure. This document is a description of JLab's Continuous Electron Beam Accelerator Facility (CEBAF), and an overview of the Hall B CEBAF Large Acceptance Spectrometer (CLAS12), alongside its major subsystems. A brief rundown of its capabilities for particle identification, tracking, and process of reconstruction is highlighted, providing important context and background as to how the detector processes data. The background physics of the elastic electromagnetic form factors, specifically the neutron magnetic form factor in the QCD is explained, motivating the measurement of the neutron detection efficiency. My research focuses on this area, providing a systematic comparison between the methodology for fitting data, to study and improve the procedures to extract the NDE.

Introduction

The Thomas Jefferson National Laboratory (JLab), is a US Department of Energy-funded accelerator facility, constructed to pioneer nuclear physics. In the late 1900s, there was significant excitement surrounding accelerator technology, and advancements in understanding fields of Nuclear physics, with investigation at many facilities such as SLAC and MIT. By 1973, the SLAC group had further developed the previous understanding of nucleonic substructure and thus dubbed the sub-atomic constituents of hadronic matter "quarks". From this, it was discovered that a more exact, complex description of hadron structure was needed, thus non-perturbative Quantum Chromodynamics (QCD) was introduced. Through the development of the Generalised Parton Distributions (GPD) regime describing the interactions between quarks within the perturbative QCD [2], physicists had to raise new questions, such as how to adequately probe a nucleon's internal structure.

In 1979, the newly formed Nuclear Science Advisory Committee (NSAC) proposed a document, dubbed the "long-range plan". This plan recognized these prior discoveries and proceeded to express a desire to investigate more thoroughly into QCD. The plan called for many advances in the current field, directly expressing a need for upgrades to previous accelerators, and an entirely new accelerator facility to investigate this. It proposed certain specific requirements and suggestions to obtain adequate funding: Firstly, a facility that produced "high energy electron beams continuously, rather than in bursts" [1] within the next two decades, as the majority of prior detectors provided bursts, and were thus unable to cover. Secondly, a realistic 2GeV minimum energy, as it is enough to resolve the gluon force interaction and reveal internal structure. And thirdly, an application of newly developed superconducting radio frequency (SRF) technology in the 1980s. The implementation of this provides a high ratio of pulse uptime to time between pulses, resulting in a high Q factor and duty factor (>80%) [4]. All components and features of which employ a high level of flexibility and future promise for upgradeability at hypothesized higher energies of >6GeV.

The Southeastern Universities Research Association (SURA) was chosen by the scientific community to oversee this new project alongside the Commonwealth of Virginia, specifying it was the "number one priority of the nuclear science community for new facilities" [4]. The Continuous Electron Beam Accelerator Facility (CEBAF) was the facility decided upon, beginning its construction in 1984. This new accelerator would ideally conform to the specifications: A continuous beam of electrons up to 4GeV, a high duty factor at a routine current of 1-150μA to the halls. CEBAF ran at 4GeV from the years 1995-2000, at which point SRF cavity technological advancements had enabled a routine 6GeV beam energy [6]. Results from this energy and previous studies at other facilities raised conflict and tension over the current understanding of quark structure within nucleons. Hence in 2002, NSAC further formally proposed a maximum energy increase to the facility, leading to CEBAF ceasing operation in 2012 in preparation for the upcoming 12GeV upgrade.

CEBAF

I - Overview

CEBAF is a culmination of efforts from multiple scientific communities and a direct result of the NSAC long-range plan proposed in 1979. Around this time, there had been developments in lattice QCD calculations: a new theory representing gluons as lattice sites and the connection between sites being represented by gluon fields, allowing for previously impossible mathematical and analytical solutions to non-perturbative QCD. These calculations indicated the existence of so-called "flux tubes" in gluons, connecting quark pairs, and describing their interactions. These interactions can only be

observed due to the weakening of the gluon force only at high energies and thus high four-momentum squared Q^2. Physicists presumed that these flux tubes when excited, would give rise to new "exotic meson states" [9] – mesons not explained by the current QCD description of two-quark bound states. GDPs are generalized descriptions of a probability density function for a particle at a specified four-momentum range Q^2, where a larger momentum reduces the resolution scale due to Heisenberg's uncertainty principle [11]. Introducing a greater kinematic range would thus allow for extending the current GPD data with greater precision and extending QCD distributions. It was decided that CEBAF would be "uniquely qualified" [8] for the express purposes of extending QCD understanding, from which point onwards, it was planned to have a beam energy of up to 12GeV, for adequately probing internal quark structure. However, due to technological restraints making such high-energy investigations "not accessible with present techniques" [1], preconcepts were put in place, requiring CEBAF to have significant leeway for future applications. With the design prospect of being an adaptable, flexible, and upgradeable facility, it has seen many upgrades and additions since its first operation in 1995 [6].

II – Electron Injection

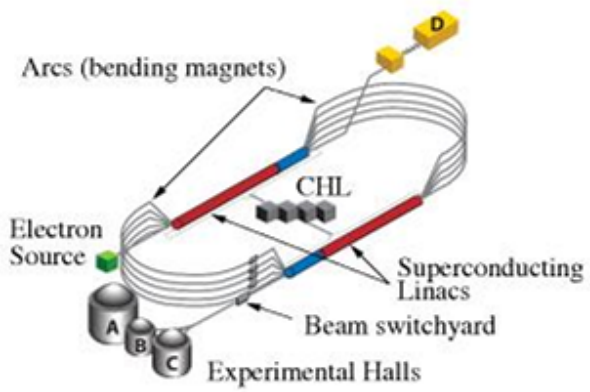

Figure 1: CEBAF general non-specific layout, showing quintessential components and major systems, from [17]

The facility continuously accelerates polarised electron bunches injected from a specialized source to an energy of 11GeV and delivers them to what was initially three halls: A, B, and C, with a final hall D, one additional half pass through the accelerator; constructed upon the 12GeV upgrade in 2017. It can be broken down into 4 subsystems, briefly shown in Figure 1. The electron injection begins with a source of 100keV GaAs (Gallium Arsenide) photocathodes that emit electrons every 2 nanoseconds at 85% polarization, set to 499MHz at 200μA total split between each hall. Figure 2 shows the full layout of CEBAF's electron injection system: Firstly, the electrons from the gun are sent through a pre-buncher cavity, separating them into bunches 250μs wide [13], before controlling total emission intensity through two apertures A1, A2. Following this is a beam chopper, which assures nominal timing by passing the bunches through three independent slits to assume a phase acceptance of 0-110ps, at 0º, 120º, and 240º separation respectively, to subsequently be bunched again. After re-bunching, the electrons are accelerated by a "graded-β five-cell cavity" [12] – similar in configuration to the cavity in figures 3.1-3.3 - up to 500keV, being further accelerated by a set of two SRF cavity sections. The first of which has two cavities, and exclusively accelerates the electrons to 5MeV as a control before farther acceleration. The second contains 8 cavities with a 14.75 MV/m field gradient, for an average of 123MeV beam energy. Throughout the injector lies magnetic elements, supplying a transverse field to the beam to control beam size, direction, and halo width. The chicane following the SRF cavities further enhances beam quality, reducing the halo by brute-forcing a reduction in the lower current region [14], the final beam is then sent to the Northern SRF Linac.

III – Beam Transport

CEBAF has two antiparallel Linacs, North and South, each being 1400m long. Both the North and South Linacs contain 25 cryomodules, with each cryomodule containing four cryounits, adding up to 8 7-cell SRF Niobium cavities, totalling 200 cavities per Linac, and ~1000 cells. During beam uptime, each cavity operates at 1497.7MHz, exactly matching

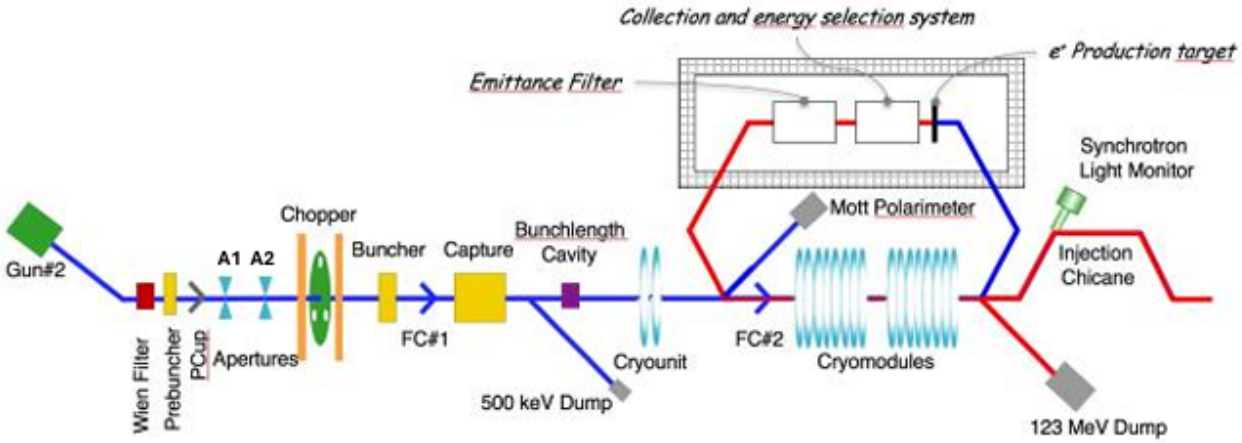

Figure 2: Electron gun preceding electron injection system at CEBAF, with all relevant components labelled, blue track shows initial path, red shows looped path through cavities from [16]

the electron injector chopper's acceptance of 499MHz per bunch, this is designed with the intent of each of the three bunches being designated one hall. Each Cryomodule is sustained at 2K by a 5kW liquid helium refrigeration system that circulates roughly 17000 gallons of liquid helium throughout the cryomodules consistently during beam uptime. CEBAF hence holds the world's largest Helium refrigeration unit for such a purpose. It is imperative for accelerator functionality that the cavities are kept superconductive at 2K using this cryogenic system, for the lost resistance and thus most efficient energy transfer. This system allows for <10mW of power to be lost per RF cycle.

Both Linacs use high-β structure for their accelerating cavities, meaning they are constructed for $\beta = \frac{v}{c} \approx 1$, and are thus commonly used for high-energy light particle acceleration, such as electron, positron, or photon accelerators. Their design is that of a series of coupled cells in which their instantaneous electron field is phase-shifted by π. As such each cell has a length of βπ/2, causing each particle to traverse one cell each half RF period [18]. Figures 3.1-3.3 show cross sections of one 5-cell cavity at CEBAF whilst an electron passes through. Each cavity has 3 stages, Figure 3.1 shows the first phase at which the electrons are accelerated by a negative charge from one side of the cell and pulled towards the other by a positive charge. Followed by Figure 3.2, where the power is cut off in preparation for when the electron approaches and reaches the next cavity, so as to not disturb its acceleration. Upon passing the cell boundary, it is shown in Figure 3.3 that the net charge is applied again but displaced by one cell to further push the electron. This process is alternated to match the frequency of incoming bunches through 5 cells in each cavity (additional 7 cell cavities were installed upon the 12GeV upgrade). Each Linac consists of a series of lattices forming a quadrupole magnet, one being placed at 9.6m intervals within the Linac, leaving a 1.35m warm region separating each 8.25m cryomodule length [6]. The lattices follow a FODO structure and are described by: F-focusing quadrupoles, D-defocusing quadrupoles, and O-drifters, acting as a focusing device for the beamline [19]. Additionally, within this region are monitoring devices to provide vital information on Linac-Linac beam phase space. Upon the end of the Linac lies a similar set of magnets for further beam control in preparation for electron recirculation through the system.

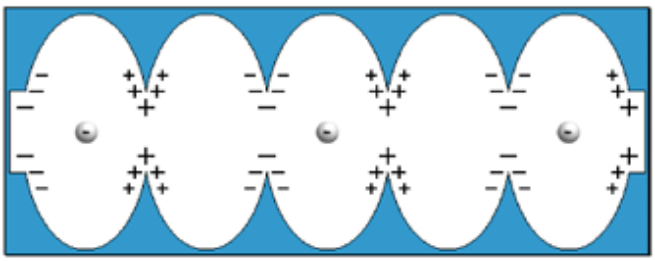

Figure 3.1: Step 1 in cavity; electron accelerated by charge distribution in cavity [17]

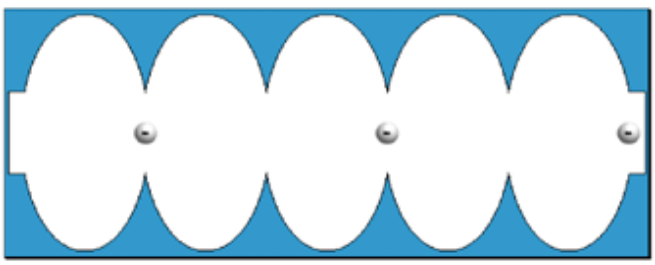

Figure 3.2: Step 2 in cavity; power switched off as electrons reach cavity separation region [17]

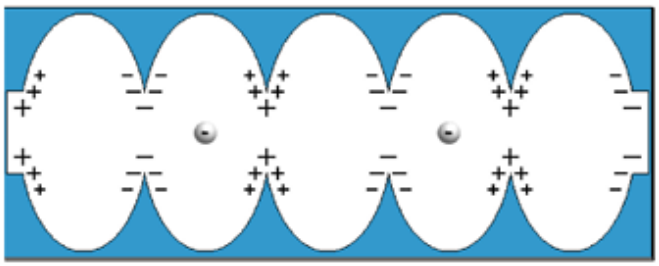

Figure 3.3: Step 3 in cavity: power re-enabled to perform same as step 1, only one cavity phase shifted [17]

Post-acceleration, the electrons exit the Linacs and begin the next stage of beam transport through the 250m arc tunnels to bend the electron beam back towards the next Linac in sequence. Figure 4 shows a top-down view of the specific logistics behind CEBAF's recirculation system, with the arcs labelled in chronological order. At the beginning of each arc are Spreaders containing dipoles applying a vertical magnetic field similar to the FODO lattices, bending the electron path upwards. The spreaders read momentum from the monitoring devices and passes are ordered to be sent first through the uppermost arcs 1S and 2S, with each circulation descending in order up until the 10th arc; a design choice made as higher energy becomes more difficult to bend. To provide a reduction in Synchrotron Radiation generated via the bending of high-energy electrons, the arcs are designed to be achromatic and isochronous, meaning the beam path is an integer of RF wavelength and is thus independent of electron energy. Thus, each electron travels at the same speed c, independent of energy [19]. Upon exiting the arc are the re-combiners labelled 1R-10R in Figure 4; they are exact mirrors of the initial spreaders and all of their components, to align the beam for re-entry into the next Linac.

The electron bunches are circulated throughout the facility and across each Linac up to a maximum of 5 repeats, with an additional pass for hall D. Upon reaching the end of their final circulation, they are met with an RF separator system at 499MHz. At which point the three 120° phase shifted bunches pass through a three-aperture electrostatic septum [18] and are sent to either hall A, B, or C: The initial bunch is left undeflected at the separator and allowed passage through the free field downstream unto hall B. Whereas the two following bunches are separated in opposite directions by performing a two-beam split and consequently extracted to halls A or C.

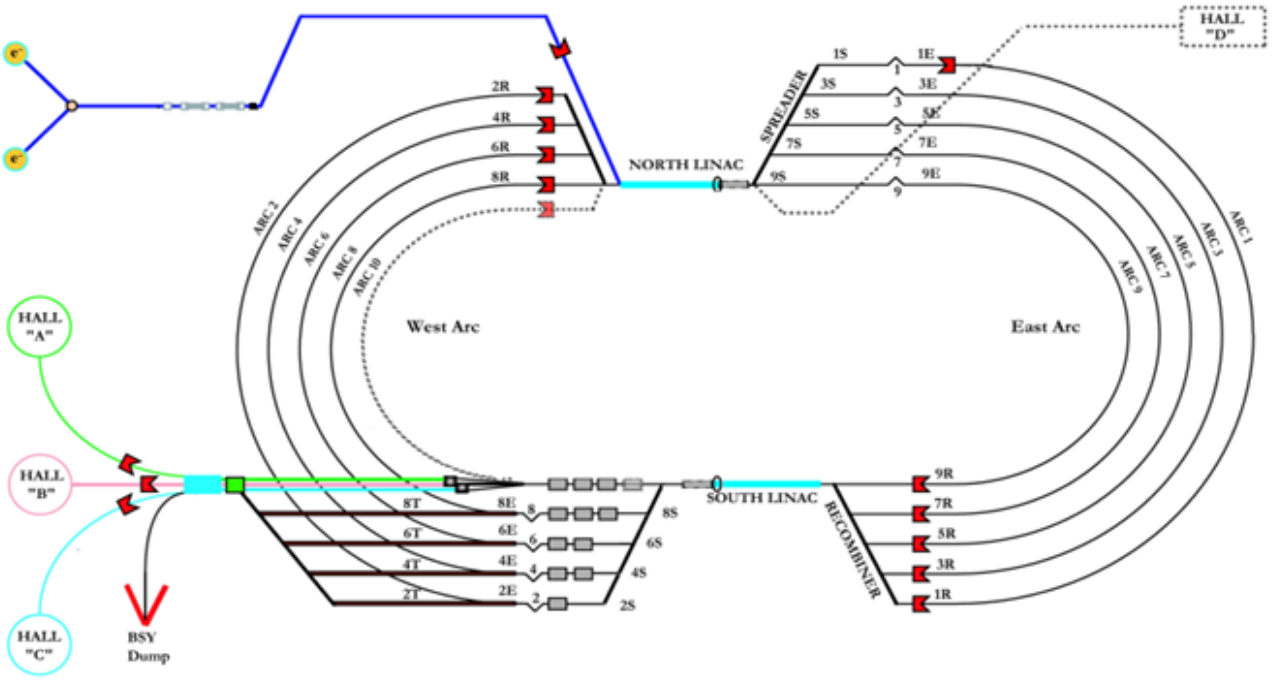

Figure 4: CEBAF top-down overview, showing specifics of only the spreader, re-combinators and magnetic steering arc information. Alongside final beam separation information upon arrival at the Halls.

CLAS12 Detector

I – Overview

In the decades before the construction of CEBAF, the discoveries of internal nucleon structure required "exclusive and semi-inclusive processes" [3], where almost all scatter products are captured, allowing for further kinematical reconstruction of baryon final states and scatter product identification. Electron accelerators in operation before CEBAF all had a small 4π solid angle and a lower sensitivity to background noise, these specifications allowed for precise measurements with the highest possible resolutions they could realistically achieve. However, these methods had disadvantages: Firstly, to obtain a high counting rate at low acceptance, the accelerators must be operated at a high luminosity, which would in turn cause a significant number of "accidental coincidences" [8]. This would restrict experimenters' access to interesting, rare scattering events due to obstructive noise from these unwanted coincidences. Secondly, low acceptance spectrometers had specifications for their target and beams, as the targets had low maximum operating currents, and beams would be limited by their total flux capacity. The main solution to these problems would be a new detector, specifically designed with the intent of capturing a large number of scattered products with a large momentum range, combined with methods of extracting necessary data from the background. With this solution in mind, and the many scientific prospects highlighted by the NSAC long-range plan [1], it was imperative to employ a high-resolution, large solid angle detector for high coincidence experiments. It was imperative to obtain a high duty factor and a higher intensity and luminosity beam for use against thin targets for the most effective scattering. This means however, that a low current halo is easy to achieve, thus the detector must operate with a low halo – allowing for the detector parts to be tighter together, increasing total angular coverage and reducing the chance to damage the components. Following these prospects, it was agreed upon that CEBAF's continuous electron beam was highly suitable for this, thus plans were made for it to be the facility at which to hold such a detector. Located directly downwards from the beamline exiting the accelerator is Hall B. This hall - being one of the three initially constructed halls - was designated to contain this large acceptance spectrometer, devoting its purpose towards a "precision study of the structure and motion of Nuclear constituents" [8]. CLAS – the CEBAF large acceptance spectrometer - was built and began its first operations and data collection in 1998. It performed within expectations and ran successfully alongside Halls A and C for 14 years, collecting significantly more data than could be fully investigated within that timeframe. All three halls ceased operation in May 2012 in preparation for the newly planned 12GeV upgrade to CEBAF. To accommodate for this new change, it was decided that CLAS be retroactively dubbed CLAS6 and that the new detector ready for the 12GeV beam would be called CLAS12. The detector has run since 2017 and is active currently, systematically it is similar to CLAS6, except intended to study at higher energy and event rates. Figure 5 shows a CAD depiction of CLAS12; the detector is shaped roughly as a cone, with the solid angle largely covered by all of its parts. There are three main systems within CLAS12, the target, the Central Detector (CD), and the Forward Detector (FD). Surrounding the Central Detector is a 5T maximum field solenoidal magnet, providing momentum for tracks within 35° to 135° polar angle around the target. The solenoidal magnet can be used for longitudinally polarized targets, providing an additional tool to study exclusive reactions or for large data collection on light nuclei targets with <90% polarization. In series with the forward detector, a torus magnet designed with 6 superconducting coils in azimuth

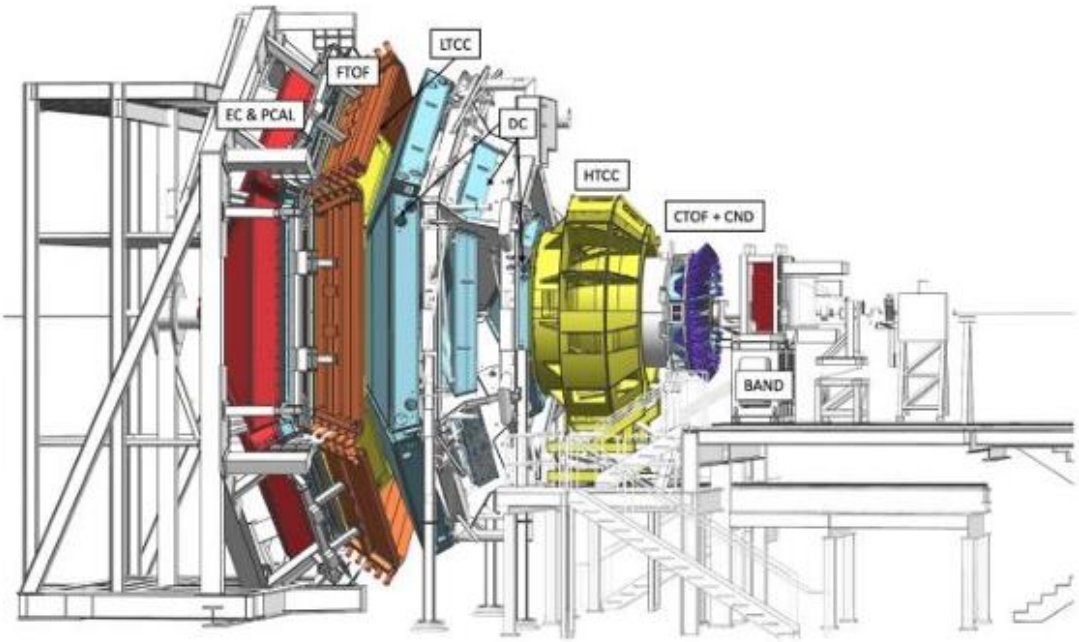

Figure 5: CAD depiction of CLAS12 Detector, with all vital subsystems and components labelled including the components of the Central detector, forward detector and target, from [20]

provides a 3.58T field, allowing for a polar tracking angle within 5º to 40º [20].

II – Central Detector

The CLAS12 Central detector can be divided into 2 main subsystems: the Central Time of Flight (CTOF), and the Central Neutron Detector (CND). Two additional systems have been added since construction: the Silicon Vertex Tracker (SVT) and a micromegas tracker (MMT), both for additional particle tracking. The CTOF system shown in Figure 6, is a 25cm wide radial detector with an effective length of 80ps at the time of an event [21]. It is located within the solenoidal magnet's confines, and outside of the central tracking system. Creating its hermetic barrel shape is 38 silicon scintillator paddles, arranged in a trapezoidal pattern to accommodate the frontmost forward detector parts. During beam uptime, the scintillators read counts via two rings of photomultiplier tubes (PMTs) positioned 1.6m radial length from each other and covered by magnetic shielding, placing them within a fringe-field region within the solenoid. Upon activation, the photomultiplier tubes measure the light and transfer it to a signal, passing through multiple stages of amplification and adjustments, and recording a count. This count allows for the identification of charged particles in the system by using the detector's 80ps resolution as a function of momentum and understanding the specific thresholds 3σ for each interaction. With thresholds of $\pi/K = 0.58GeV$, $K/\rho = 0.95GeV$, and $\pi/\rho = 1.14GeV$, the CTOF can identify pions, kaons, photons, and electrons at the beginning of an event in CLAS12. As seen in Figure 6, the CND system surrounds the front-most section of the CTOF and is 5cm radial distance farther from the beamline. It is similar in shape, with 48 segments of 3 layers, adding to 144 scintillators and 144 PMTs with a time resolution of 150ps. Its purpose is to detect neutrons within 40º to 80º polar

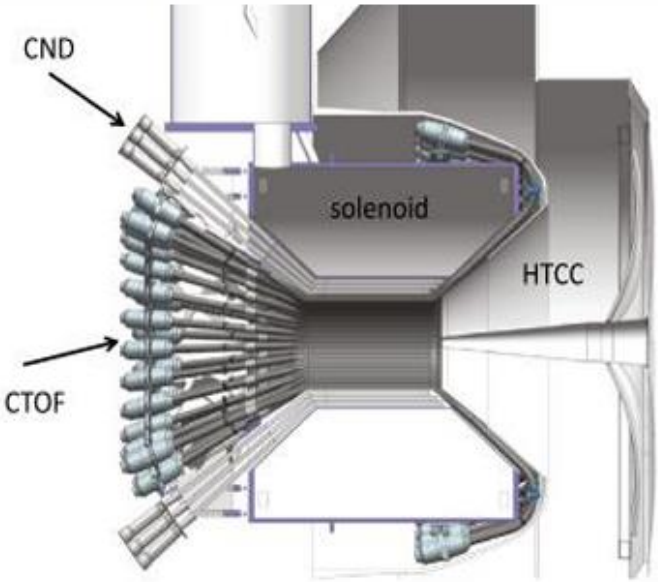

Figure 6: Croll section of Central detector showing only Central Time of Flight CTOF, Central Neutron Detector CND, the solenoid and the Forward Detector's High Threshold Cherenkov Counter HTCC, from [21]

angle and a kinematic range of 0.2GeV to 1.2GeV. Distinguishing a Neutron can be determined by comparing the TOF of the particle against its flight path from the CTOF detector and z-axis radial geometry of the scintillator bars. In addition to this, the CTOF can also distinguish neutrons using the same methodology, adding 3-5% [21] of detection efficiency to the system.

III – Particle Identification

The CLAS12 Forward detector is 7m long, with 6 sectors based around the six-coil torus magnet and can be divided into 5 main subsystems downstream from the target, that work to provide pivotal information for the particle identification and tracking within the detector. Located just in front of the Central Detector is the first component of the forward detector: the High Threshold Cherenkov Counter, the first of two Cherenkov counters in the Forward Detector, and one of five particle identification subsystems in CLAS12. This system is used for the detection of electrons in a scattering event, and the electron separation from charged pions and kaons. Its geometry is that of an ellipsoidal multifocal mirror, consisting of 48 total mirror facets: 12 half sectors, each with 4 mirror subsections. It has 360° coverage in azimuth – meaning all scatter products along the horizontal reference plane are captured. Additionally spanning a polar angle of 5° - 35° [23], allowing for adequate coverage at this frontmost stage. Each mirror focuses Cherenkov light through to 48 total PMTs shielded from the torus by mild-steel magnetic plating. R&D engineered the HTCC with design prospects of providing maximal strength to the structure without internal support interference and retaining a lightweight frame, in addition to consuming a minimal amount of active area around the other tracking components. It operates with a dry Carbon Dioxide gas working at room temperature (25°C) and at 1 atmosphere. As electrons pass through the Carbon Dioxide volume, they are moving more quickly than the effective speed of light in said medium, releasing Cherenkov radiation in the forward direction of the particle's trajectory in a Cherenkov cone with an angle of reflection given by $\theta_c = cos^{-1}\left(\frac{1}{\beta n}\right)$ *where* $\beta = \frac{v}{c}$. The 48 mirrors reflect this spread of radiation onto focal points and light cones on and around the PMTs, where it is collected and electronically translated through CLAS12's reconstruction system. The system rejects any readings above a 4.9GeV threshold as they are identified as non-electrons as per a preset calibration. Located toward the rear end of the Forward Detector is the 2nd of two Cherenkov Counters: the low-threshold Cherenkov Counter (LTCC). Geometrically, it differs significantly from the HTCC's design, consisting of 108 mirror sections in each of the 6 CLAS12 sectors, each sector containing 36 PMTs alongside the prerequisite light collecting cones and magnetic shielding for each, with the configuration being shown in Figure 7. It operates with a denser C_4F_{10} (Perfluorobutane) gas medium than the CO_2 in the HTCC, instead allowing for a pion/kaon separation threshold in the range of 3.5-9GeV. Thus, working with the HTCC, the LTCC further assists with identifying scattered products in the forward detector by providing this pion/kaon separation energy during each event.

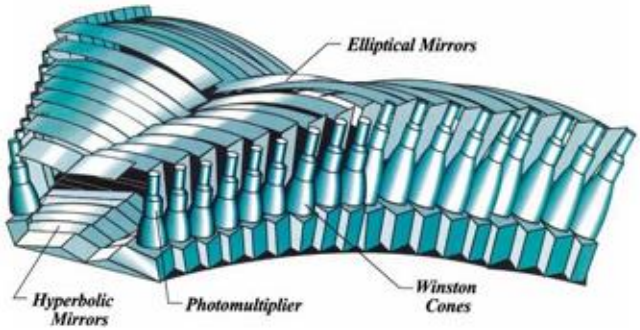

Figure 7: CAD diagram of one of the six sectors from the Low-Threshold Cherenkov Counter LTCC in CLAS12 from [24]

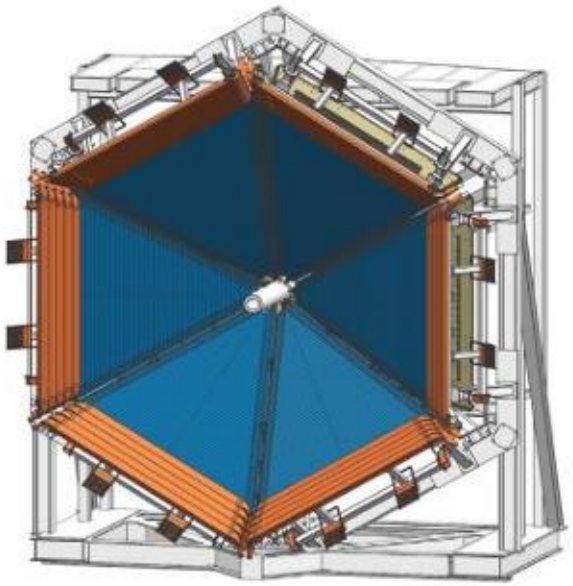

Figure 8: CAD model of Forward Time-of-Flight FTOF, showing sectors. Dark blue scintillators are panels 1a and 1b, orange is panel 2, from [27]

The third identification subsystem in CLAS12 is the Forward Time-of-Flight (FTOF), positioned in Figure 5, as the second to last major subsystem along the beamline. The FTOF is the primary subsystem for particles up to ~5GeV [27], and much like the CTOF in the central detector, it measures with an active time resolution of σ=80ps at angles <35°, increasing to 150ps at angles >35° up until the polar limit of the forward detector. Its construction is that of straight scintillator bars, lined radially outwards from the beamline, with PMTs at each end of each scintillator, including a "shadow region" [27] defined by a fiducial cut for a 50% azimuthal acceptance at low angles, and 95% at greater angles. Each of its 6 sectors contains 3 Panels, Panel-1a, Panel-1b, and Panel-2. Panels 1a and 1b cover the tighter angle, with a resolution range of 90-180ps and 60-110ps over their 23 and 62 counters respectively, averaging 80ps resolution in conjunction. Whereas Panel-2b has only 5 counters for the additional acceptance at a greater polar angle. Identification is performed by using a time difference of 4σ (0.32ns) as a function of momentum to define the threshold for particle species. These thresholds being: π/K = 2.8GeV, K/ρ = 4.8GeV and π/ρ = 5.4GeV.

At the farthest point in the forward detector down the beamline lies the final stage in particle identification, a set of calorimeters: the Electromagnetic Calorimeter (ECAL) at the rear, salvaged from CLAS, and the Pre-shower Calorimeter (PCAL) in front of the ECAL, newly implemented for CLAS12. The purpose of both calorimeters is the kinematical reconstruction of electrons and neutral particles, typically photons and neutrons. Both ECAL and PCAL contain

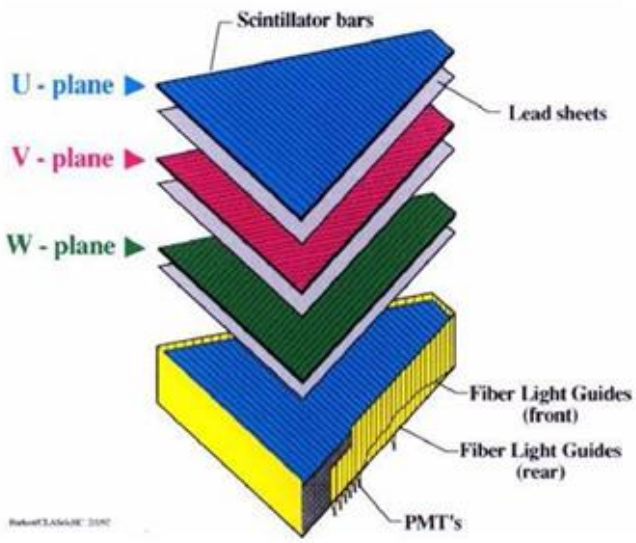

Figure 9: Exploded diagram of one of the six sectors of the Electromagnetic Calorimeter EC, showing U, V, W scintillator planes separated by lead sheets, in-line with optical fibre guides and PMT readouts, from [28]

alternating layers of 3-directional scintillator bars separated by 2.2mm thick lead sheets for scattering between each layer. Figure 9 shows an exploded assembly of the sections of the EC, with each U, V, and W plane forming a hodoscope layout by alternating 36 scintillator bars parallel with each side of the triangular sections. There are 39 total layers of scintillator material per sector, with signals combined in 15/24 layers and routed through optical fibres to 2 PMTs respectively, named ECAL-inner and ECAL-outer. The PCAL follows the same geometry, albeit containing 84/77/77 scintillator bars in the U/V/W layers respectively instead. The innermost 52/46/46 bars in U/V/W have quartz fibre guides to one readout PMT each, and the outermost 32/33/33 have one readout PMT per 2 bars, totalling 68/62/62 PMTs per sector, condensing into a total of 5/5/8 readout views for the PCAL/ECAL-inner/ECAL-outer. These readout numbers were chosen based on improving the electron/hadron separation by providing a longitudinal sampling as opposed to a singular readout for each layer and incidentally, reducing manufacturing and runtime costs [28]. The specifications for these detector parts such as the momenta threshold of the TOF detectors - alongside other specifically manufactured components such as the width of the PMTs and scintillator bars in the PCAL - are generated from a series of CLAS12's Geant4 simulations done before assembly and manufacture.

IV – Particle Tracking

To be able to fully track and recognize particles from the large kinematic range CLAS12 provides, a precise, large polar angle tracking system is needed to match the larger momenta and thus tighter angles a large number of particles take during operation. To perform this, as the particles leave the HTCC, they begin interacting with the toroidal magnetic field in the Forward Detector and are sent through a set of Drift Chambers. The Drift Chambers are used for the tracking of charged particles through CLAS12 and are part of the "forward tracker"[25] system in assembly with the torus. There are 3 separate multi-layer Drift Chamber sections R1, R2 and R3, separated into 6 equilateral triangle sectors, with 2 superlayers per sector, each containing 6 layers of wiring, the remaining space being occupied by a 90:10 CO_2 and Argon mixture gas medium. The separation of layers results in 112 parallel hexagonal cells per layer of wire arranged into a "brick wall" [25] pattern. This pattern places a layer of guard wires at the front and rear end of the superlayers, followed by a field-field-sense-field-field-sense pattern repeating until the outmost guard layer is reached, being finally met with a set of non-conducting endplates on either side, used for the tensioning of wires, to reduce eddy currents and force distributions [25]. The chamber's total architecture was designed to minimize dead areas between the endplates and electronics, thus maximizing the active volume of the chambers, torus, and wiring. Further design specifications place the superlayer chambers at ±6° to the sector geometry, the frontal superlayer at +6°, and the rearmost superlayer at -6°. This angle difference allows for an increase in overall polar resolution compared to having each layer at the same angle. Separating the layers into chambers additionally allows for easier maintenance should wires break or faults occur. Each superlayer is supplied by one of two High Voltage Translator Boards (HVTBs) by connections on the endplates, with each wire (guard, sense, field) being supplied by a different voltage from these HVTBs. Upon an interaction along a sense wire, a small current is transmitted across a Signal Translator Board (STB) with an inbuilt Single Inline Package (SIP) preamplifier, where it is amplified, extended, and further transmitted downstream, at which point it is further amplified, and converted to a digital time signal. These signals from the forward tracker in the toroidal region, provide enough tracking information to reconstruct the paths of charged particles in CLAS12.

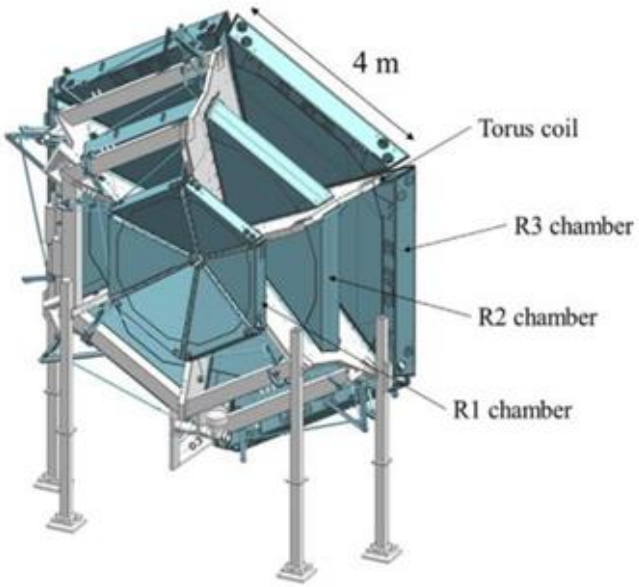

Figure 10: CAD model of Drift Chambers R1, R2, R3, showing the intrinsic architecture between each sector, alongside the torus magnet, from [25]

V – Event Reconstruction

Each time an electron bunch hits the target nucleus, it causes a reaction where particle products pass through the subsystems in the central and forward detectors. During an experiment, the event data is collected and stored for reconstruction and extraction, performed for each particle's 4-vectors within a collision. Firstly, each subsystem is isolated and performs hit-based-tracking (HBT) reconstruction, the process is executed differently depending on the methods each subsystem employs. The Event Builder then performs time-based-tracking (TBT), by combining all of the isolated HBT information and processing it. Finally, the software reruns the whole analysis, this time with the HBT and TBT information already collected, allowing for certain subsystems to perform additional functions, greatly increasing the resolution and precision of the data.

The hit-based tracking starts when the raw data is processed by different algorithms within each detector subsystem. Firstly, through the Cherenkov light collected and processed within the HTCC electrons/pions/kaons are identified. There are three stages to signal reconstruction: firstly, the signal strength from the PMTs is amplified from the raw HTCC::ADC databank channels and determined by signal threshold crossing time subtracted from the pedestal [23], both stored in the Jefferson lab's calibration constant database (CCDB) [28]. Each signal is converted into several photoelectrons from gain constants in the CCDB given by: $nphe_{hit} = \frac{ADC}{gain}$, which also allocates angular coordinates of the hit. The geometry of the HTCC results in each hit splitting into up to four channels, these split signals are combined into a cluster to begin reconstruction of the unaltered signal. The largest photoelectron signal is chosen as the starting "seed' for this cluster, each hit within an adjacent calibrated time window being added to this cluster, ignoring hits outside this window. Signal strength is thus determined by a summation of individual signals as a weighted average of the number of photoelectrons from the PMTs. The algorithm then iterates over a list of all hits and a projection of the completed cluster is sent back onto the mirror surface within the HTCC, providing coordinates on the location of the real hit and storing it in an HTCC::clusters databank.

Event reconstruction also requires data from the calorimeters. Raw data is collected from the scintillator layers upon a hit, and each of the 5/5/8 PMT readout channels within the ECAL and PCAL provides pulse information based on total energy deposited within a collection of the U, V, and W layer strips, overlapping into a "stack". Thresholds within the CCDB define at which point the cluster-finding algorithm groups individual stacks into a peak, making further use of the scintillator geometry to subdivide peaks into hits based on the energy profile provided by each stack. The sum of the peaks from each U, V, and W layer defines a cluster and is used to determine its energy over a 10MeV threshold [28]. A cluster location is determined by a series of Line-of-closest-distance measurements between U and V peaks, the midpoint of the UV line, and a cut along the UV-W distance. Transverse coordinates within the z' frame (depth into the scintillator layers) are determined by the midpoint of the UV-W distance

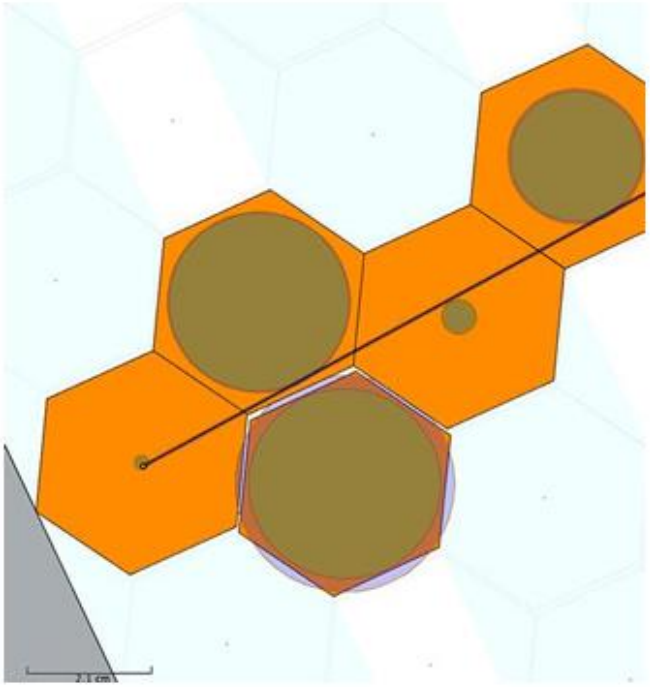

Figure 11: Cross section of the sense wires and hexagonal cells, illustrating time-based tracking of the one of the drift chamber DC superlayers, green circles show the distance of closest approach from Hough transforms that the track candidate(black line) takes, from [28].

cut. The largest energy weight average peak from the data is taken alongside the peak timing - corrected for light propagation - to evaluate the cluster's localized timing.

The double-ended PMT readouts from the FTOF and CTOF detectors give raw flash ADC and TDC hit and time data, taken above a 1MeV threshold with a timing resolution of ~1ns. Data of which is chosen from a 10ns time window. Through a subtraction of time-walk corrections, light travel time, and a channel-to-time conversion factor, the hit time can be obtained, with coordinates given by: $y = \frac{v_{eff}}{2}(t_1 - t_2 - C_{12})$, where v_{eff} is the effective velocity and C_{12} is the time offset to the centre of the TDC distribution, obtained from the CCDB. These coordinates allow the matching of the TOF to a projected track obtained from the forward tracking reconstruction algorithms. Both panels 1-a and 1-b in the FTOF can have their clusters matched to determine whether they originate from the same track, if so a weighting of the time resolution is applied as a correction, leading to an effective time resolution increase of 15-20% through cluster matching.

The Drift chambers provide pivotal hit-based tracking information that is processed in two stages, followed by a pattern recognition algorithm. Hit reconstruction begins by defining a signal as a representation of a geometric object within the detector. The lab employs a Simple Noise Removal (SNR) algorithm, where uncorrelated noise is filtered from the system, allowing for preliminary track reconstruction. Raw preliminary hits do not provide any timing information, so corrections to the final drift time are applied from information provided by the time-based tracking after initial data collection. The time-of-flight detectors, event start and end time values from the HTCC and LTCC, alongside time delays

and time propagations from the wire itself, summed with this timing information. From this, a distance-of-closest-approach method is employed as seen with the green circles in Figure 11. Clusters are formed within each DC superlayer from adjacent hits within each wire layer, up to two maximum hits per layer. Algorithms recognize high-momentum tracks and split the clusters into overlapping segments, followed by fitting a linear straight-line hypothesis and saving it for later evaluation. A 6-dimensional "cross" [28] object is employed between adjacent superlayers to evaluate line coordinates of plane intersections caused by saved tracks. A pattern recognition algorithm searches for three adjacent crosses between each of the three DC regions using a parabolic fitting function, labelling such a scenario as a "track candidate". Preliminary charge momentum parameters for track fitting uses a track candidate as a base, and are computed through a comparison of the cross angle between the first and third DC regions R1 and R3 given by: $\frac{q}{p} = \frac{\theta_3 - \theta_1}{v \int Bdl}$, where $\int Bdl$ is the magnetic field intensity along the track trajectory. Tracks for fitting are represented by 5 parameters (x, y, tx, ty, Q) within a z-coordinate system (the cross-section of wire planes). Expressing the hit state vector as derivates with respect to z, and through an application of a fourth-order Runge-Kutta integral method across each superlayer, allows for propagation along the DC z plane. From this time, the drift distance is computed via a set of time-to-distance arrays, and the fit is redone for the now completed distance as an additional measure of accuracy. The track parameters are converted into the lab frame (x, y, z, px, py, pz), and the equations of motion of the particles are computed from "swimming" the tracks [28]. This is repeated for each vertex as a final propagation to match the intersection with each detector surface and to match the clusters of the other tracking subsystems. After algorithmic processing from each subsystem, the data is stored in a collection of 5 databanks: tracks, trajectory, clusters, hits, and moments. CLAS12's event builder (EB) service collects these banks and compiles a new set of relevant reconstructed (REC) banks: Event, Particle, Calorimeter, Cherenkov, Scintillator, and Track. This data is now fully processed and ready for experimental analysis using the myriad software tools Jefferson Lab provides, such as COATJAVA or CLAS12's Common Tools.

Research Focus

I – Scientific Motivation

A major, fundamental problem in nuclear physics is the understanding of the form factors of nucleons, which has been further developed since the introduction of the generalized Parton distribution in terms of the QCD. Within the QCD, the form factors; $G_E^n, G_M^n, G_E^p, G_M^p$, are quantities that describe nucleon quark structure, alongside internal current and magnetization distributions, extending a motivation towards multiple aspects of nuclear physics. Through understanding these elastic and magnetic form factors we can fully unravel the individual contributions from up and down quarks. Further increasing the understanding of general quantum field theory, the dressing of quarks and quark

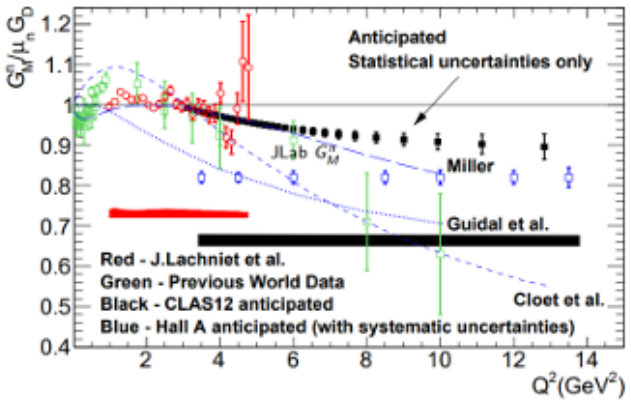

Figure 12: Plot showing world data on the neutron magnetic form factor, including newly anticipated data from recent CLAS12 data, from [30].

confinement [31] within the perturbative QCD. The common method of obtaining nucleon form factors is through high energy electron scattering, as previously mentioned in the NSAC long-range plan [1], the Jefferson Lab provides the optimal conditions for performing such methods. The lab first showed interest in form factors in 1998, with the introduction of a new technique of determining the form factor, using a ratio of the cross sections – essentially a ratio of ratios. Currently, this method is employed at CLAS12 to determine the neutron magnetic form factor, the most difficult form factor to decipher due to the short-lived neutral nature of neutrons. Through careful event choice selection and an understanding of the other constituent form factors of nuclei, this can be found.

$$R = \frac{\frac{d\sigma}{d\Omega}(^2H(e,e'n)p)_{QE}}{\frac{d\sigma}{d\Omega}(^2H(e,e'p)n)_{QE}} \quad (1)$$

$$G_M^n = \sqrt{\left[\frac{R}{a(Q^2)}\left(\frac{\sigma_{mott}^p}{\sigma_{mott}^n}\right)\left(\frac{1+\tau_n}{1+\tau_p}\right)\left(G_E^{p\,2} + \frac{\tau_p}{\tau_n}G_M^{p\,2}\right) - G_E^{n\,2}\right]\frac{\epsilon_n}{\tau_n}} \quad (2)$$

Equation 2 above gives the neutron magnetic form factor, calculated from the ratio of cross sections R given by equation 1. In addition to this, certain experimental corrections $a(Q^2)$ are applied, the proton and neutron cross-sections σ_{mott}^n and σ_{mott}^p are substituted, alongside kinematic variables extracted from information provided by the detector τ_n, $\tau_p$and ϵ_n [30]. Equation 2 shows two different events, showing e-n over e-p scattering, made possible through manually selecting data of these specific scatter products. Through the usage of a deuteron target, Neutron and Proton events can be selected simultaneously. There are multiple advantages to this: firstly, measurements of both neutrons and protons at once allows for a significant mitigation of nuclear correction factors, which would otherwise be necessary had the measurements been taken separately. Secondly, it removes the need to take a total count of electrons for each event, as the separate events share counts. Thirdly, the swimming of the protons and neutrons allows for acceptance matching – events with both proton and neutron hits at the same time thus lie within the same solid angle, removing an additional corrective factor, and allowing for less intensive calculations.

II – Neutron Detection Efficiency

The current ratio methodology to determine the neutron magnetic form factor requires a measurement of the number of the e-n events as a function of Q^2 and thus requires neutron measurements as it makes use of the neutron cross-section seen in equation 2. However, the CLAS12 detector has only the ability to reconstruct the tracks of charged particles. This means that the calorimeters cannot detect neutrons at 100% efficiency, thus a rudimentary "neutron detection efficiency" must be calculated. Tracking neutrons begins with choosing a proton target, as it is stationary and allows for less complex tracking. Firstly, events with scattered electrons, pions, and neutrals are searched for, assuming the only neutral hits are neutrons using the event choice denoted by $H(e,e'\pi^+)n$. Information on the electron and pion from the reconstruction process is used with the laws of momentum conservation to find the neutron's momentum, allowing for a calculation to be done to generate a region of expected neutron hits. If the event hits CLAS12's active region, the detected neutral hits within the calorimeter are collected, and a track is swum back to the target vertex. This track is trivial to calculate, as the neutrons will not be affected by the toroid, and therefore follow a straight line. Within the z-sector coordinate system, a plot of the direction cosines is calculated by each momentum component over the total momentum, given in Figure 13, showing a clear peak of neutral hits within the calorimeter. Finally, a difference in the number of expected hits over the number of detected neutral hits is taken and the Neutron Detection Efficiency can be calculated by equation 3.

$$NDE = \frac{H(e,e'\pi^+n)}{H(e,e'\pi^+)n} \quad (3)$$

In the 6GeV era, the ECAL had an NDE of ~60%, as shown in Figure 14. Upon the upgrade to 12GeV in 2017, and with the addition of the pre-shower calorimeter PCAL, more work has been done on the NDE and it has seen an overall increase up to ~80% . Meaning current readings for neutrons require a multiplier of 1.2x to be applied, to correct for the detector's inability to detect 20% of the scattered neutrons.

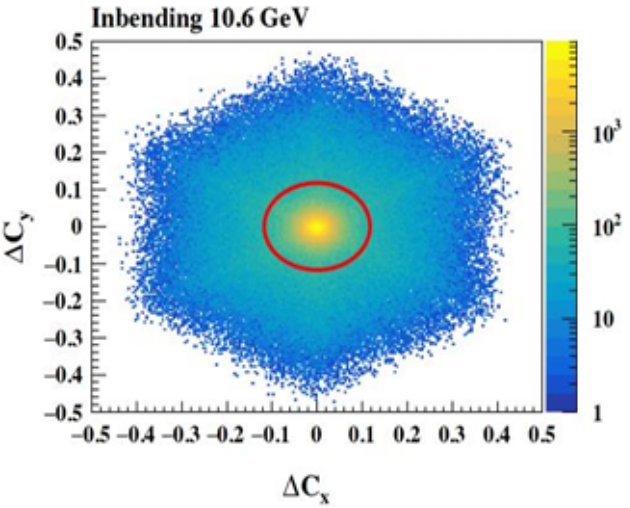

Figure 13: Plot of differences in direction cosines, used for determining the cut to take when searching for detected neutrons on the calorimeter, from [32]

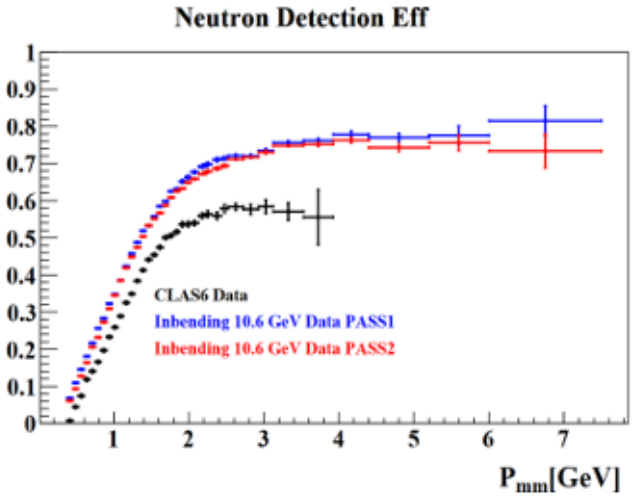

Figure 14: CLAS6 data) on the Neutron Detection Efficiency, showing two beam energies, resulting in a ~60% efficiency, from [33]. CLAS12 data, showing in bending and out bending at 10.6GeV from a crystal ball and 4th order poly.

III – Research Goals

Currently, the work done on the magnetic form factor of the neutron requires the NDE, thus any improvement to this value will be an improvement to the precision of the form factor measurement. Work done on the NDE with CLAS in the 6GeV era was performed on a significant amount of data over a low energy range. CLAS12 however, has far greater statistics due to a higher energy range, significantly increasing the total background noise in the data, a comparison shown in Figure 14. Work performed on CLAS did not require modelling of the fit of the missing mass as seen in [33] due to the lower background whereas measurements on CLAS12 in 2023 require a fitting of the missing mass through a crystal ball function, summed with a fourth-order polynomial to model the background. This leads to the main focus of my research, namely an investigation into the fitting methods used for determining the neutron detection efficiency of the calorimeters at CLAS12.

A crystal ball function is a fitting function commonly used with modelling in high-energy particle physics. It consists of a Gaussian core, combined with a power-law tail. A crystal ball function with a fourth-order polynomial background, where it has parameters $\bar{x}$, σ, α, and n, which manipulate the mean of the Gaussian, the width of the Gaussian, the starting point of the tail, and the normalization factor of the tail respectively.

$$f(x;\alpha,n,\bar{x},\sigma) = N \begin{cases} \exp\left(-\frac{(x-\bar{x})^2}{2\alpha^2}\right), & for\ \frac{x-\bar{x}}{\alpha} > -\alpha \\ A\left(B - \frac{(x-\bar{x})^2}{\alpha}\right), & for\ \frac{x-\bar{x}}{\alpha} \leq -\alpha \end{cases} \quad (4)$$

$$A = \left(\frac{n}{|\alpha|}\right)^n exp\left(-\frac{|\alpha|^2}{2}\right), \quad B = \frac{n}{|\alpha|} - |\alpha| \quad (5),(6)$$

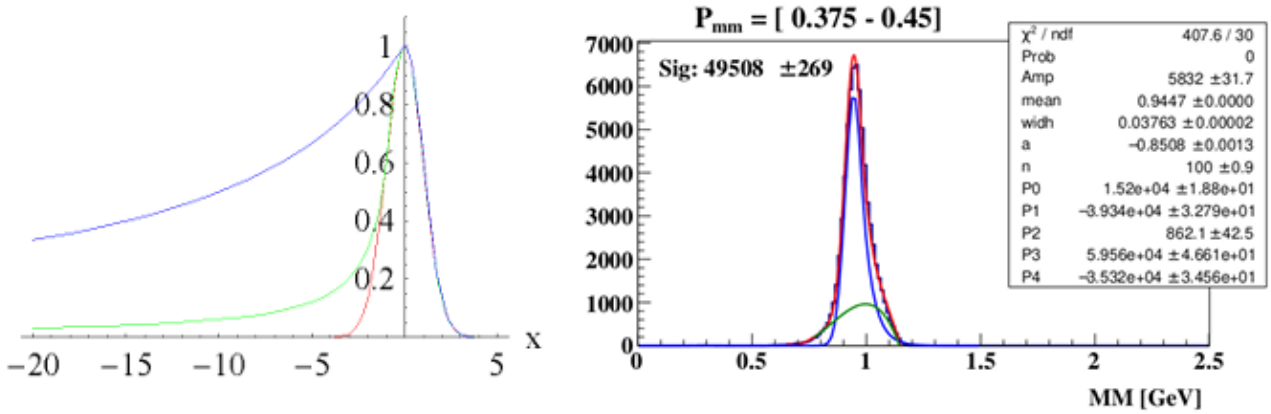

Figure 15: (left) Simple example of a crystal ball function with parameters $\bar{x}$=0, σ=1, n=1, blue α=0.1, green α=1, red α=10, showing the effect parameterization has on overall results, from [34]. (right) Crystal Ball Fit for expected neutron bin, done with in-bending 10.6GeV beam data, showing increasing parameter complexity with real data fitting.

Equations 4, 5, and 6 show a crystal ball function, and Figure 15 shows them graphically, with the simplest form of parametrization. These parameters are unit-defined and must be manipulated precisely when fitting. As shown, the smallest modification to a parameter can wildly influence the function's shape and form. Figure 15 is the simplest scenario when working with the tens of millions of events CLAS12 provides, and when introducing significant background, it becomes imperative to control the parameterization realistically and carefully to be a realistic fit. This brings up the possible idea of applying a systematic approach to the fitting of data for determining the neutron detection efficiency. This could be done via a modification to the current function parameterization and fitting algorithm. An introduction of a new function with similar capabilities such as a double crystal ball function – a crystal ball function with a tail on both sides – with retaining previous parameters, modifying existing ones, introducing new ones, or possibly testing symmetry and asymmetry systematically between methods, could be a valid approach. These changes would entail significant comparison between methods, to provide a visual representation of the difference in results and the overall impact it has on the NDE. In addition to this, providing a low-labor investment into this work would highly benefit the lab and its goals, thus this work could automate the process of fitting the NDE.

Summary

Since its construction in 1995, the Jefferson lab has been on the frontier of nuclear physics research, providing never-before-seen insight into the QCD. It was designed with this in mind for the future, constructing CEBAF for the pioneering of high energy particle physics with its continuous electron beam, and constructing CLAS12 with the aspiration of a detector capable of capturing scatter products at a wide angular range and a large acceptance, allowing for the capture of scatter products a large 4π solid angle. Through the usage of CLAS12, the lab has been able to investigate more complex, specific areas of the QCD, namely nucleons, nuclei, and their 3D images. It does this by making use of CEBAF's capabilities, and by using a culmination of the many major subsystems within the detector, contributing to particle tracking, identification, and reconstruction. The lab employs this reconstruction process when searching for neutrons, to determine the difficult to decipher neutron magnetic form factor from the e-n/e-p ratio method. Due to the nature of CLAS12, the system has a specified neutron detection efficiency that must be calculated through careful fitting of missing mass distribution in many neutron momentum bins and hence used to extract the neutron magnetic form factor. My research aims to investigate the fitting methods employed by researchers at the lab and utilize a systematic approach to comparing the differences generated, ideally automating the process for the lab's future convenience.

Acknowledgments

This Project and Research is supported and funded by the United States Department of Energy (DOE) and is affiliated with The University of Richmond and the Thomas Jefferson National Laboratory. Thank you to JLab Staff Veronique Ziegler for supporting my program and thank you to Professor Gerarde P. Gilfoyle for supervising my project and organizing my research alongside Postdoc Lamya Baashen.

Bibliography:

[1] Robinson, A.L. (1980). A Long-Range Plan for Nuclear Science. *Science*, 210(4475), pp.1236–1237. doi:https://doi.org/10.1126/science.210.4475.1236.

[2] Riordan, M. (1992). The Discovery of Quarks. *Science*, [online] 256(5061), pp.1287–1293. doi:https://doi.org/10.1126/science.256.5061.1287.

[3] Burkert, V. Et al. (2020). The CLAS12 Spectrometer at Jefferson Laboratory. *Nuclear Instruments and Methods in Physics Research Section A: Accelerators, Spectrometers, Detectors and Associated Equipment*, 959, pp.163419–163419. doi:https://doi.org/10.1016/j.nima.2020.163419.

[4] Westfall, C., 1994. *The Founding of CEBAF 1979 to 1987,* Michigan State University: Southeastern Universities Research Association.

[5] Whitney, R. R., October 1984. *The SURA/CEBAF project,* Newport News: Springer-Verlag, Heidel-berg.

[6] Leemann, C., Douglas, D.R. and Krafft, G.A. (2001). The Continuous Electron Beam Accelerator Facility: CEBAF at the Jefferson Laboratory. *OSTI OAI (U.S. Department of Energy Office of Scientific and Technical Information)*.

[7] Nuclear Science Advisory Committee, 2002. A Long-Range Plan for the Next Decade. *Opportunities in Nuclear Science,* p. 159.

[8] CONCEPTUAL DESIGN REPORT BASIC EXPERIMENTAL EQUIPMENT ELECTRON BEAM ACCELERATOR FACILITY RECEIVED. (1990). Available at: https://digital.library.unt.edu/ark:/67531/metadc674902/m2/1/high_res_d/491625.pdf [Accessed 12 Jun. 2024].

[9] Hardwood, L., 2003. *Upgrading CEBAf to 12 GeV.* Newport News, 2003 Particle Accelerator Conference. Available at: https://ieeexplore.ieee.org/stamp/stamp.jsp?tp=&arnumber=1288982 [Accessed 12 Jun. 2024].

[10] Chao, Y., Drury, M.I., Hovater, C., Hutton, A., Krafft, G., Poelker, M., Reece, C. and M. Tiefenback (2011). CEBAF Accelerator Achievements. *Journal of physics*, 299, pp.012015–012015. doi:https://doi.org/10.1088/1742-6596/299/1/012015.

[11] Ji, X. (2013). Parton Physics on a Euclidean Lattice. *Physical Review Letters*, 110(26). doi:https://doi.org/10.1103/physrevlett.110.262002.

[12] Kazimi, R., Benesch, J.F., Chao, Y., Grames, J.M., Krafft, G.A., M. Tiefenback, B.C. Yunn and Zhang, Y. (2006). Injection Options for 12 GeV CEBAF Upgrade. *Proceedings of the 2005 Particle Accelerator Conference*. doi:https://doi.org/10.1109/pac.2005.1591311.

[13] Sinclair, C., 1992. A 500kV photoemission electron gun for the CEBAF FEL. *Nuclear Instruments and Methods in Physics Research*, 318(1-3), pp. 410-414.

[14] Kazimi, R. et al (2004). CEBAF injector achieved world's best beam quality for three simultaneous beams with a wide range of bunch charges.

[15] Wang, Y., 2010. *CEBAF Overview,* Newport News: s.n. Available at: https://www.jlab.org/hugs/archive/Schedule2010/slides/Wang.pdf [Accessed 13 June 2024]

[16] A. Camsonne, M. C. R. E. J. G. e. a., 2020. *Deeply Virtual Compton Scattering,* s.l.: Neutral Particle Spectrometer Collboration. Available at: https://www.jlab.org/exp_prog/proposals/20/PR12-20-012_Proposal.pdf [Acessed 13 Jun 2024]

[17] Gilfoyle, G. P., n.d. *Hunting for Quarks.* [Online] Available at: https://facultystaff.richmond.edu/~ggilfoyl/research/researchIntroS23.pdf [Accessed 11 June 2024].

[18] Padamsee, H.S. (2014). Superconducting Radio-Frequency Cavities. *Annual Review of Nuclear and Particle Science*, 64(1), pp.175–196. doi:https://doi.org/10.1146/annurev-nucl-102313-025612.

[19] Bodenstein, R. M., 2012. *A Procedure for Beamline Characterization and Tuning in Open-Ended Beamlines,* s.l.: Univeristy of Virginia.

[20] Jefferson Lab, 2017. *Experimental Hall B.* [Online] Available at: https://www.jlab.org/Hall-B/int-web/welcome.html#:~:text=CLAS12%20Spectrometer,-The%20new%20CEBAF&text=The%20construction%20of%20the%20detector,event%20rates%20compared%20to%20CLAS. [Accessed 13 June 2024].

[21] Carman et al (2020). The CLAS12 Central Time-of-Flight system. *Nuclear instruments and methods in physics research.* pp.163626–163626. doi:https://doi.org/10.1016/j.nima.2020.163626.

[22] P. Chatagon et al (2020). The CLAS12 Central Neutron Detector. *Nuclear instruments and methods in physics research. t,* 959, pp.163441–163441. doi:https://doi.org/10.1016/j.nima.2020.163441.

[23] Y.G. Sharabian et al (2020). The CLAS12 high threshold Cherenkov counter. *Nuclear instruments and methods in physics research.* 968, pp.163824–163824. doi:https://doi.org/10.1016/j.nima.2020.163824.

[24] Ungaro, M et al (2020). The CLAS12 Low Threshold Cherenkov detector. *Nuclear instruments and methods in physics research.* 957, pp.163420–163420. doi:https://doi.org/10.1016/j.nima.2020.163420.

[25] Mestayer, M.D et al (2020). The CLAS12 drift chamber system. *Nuclear instruments and methods in physics research.* 959, pp.163518–163518. doi:https://doi.org/10.1016/j.nima.2020.163518.

[26] Carman, D.S et al (2020). The CLAS12 Forward Time-of-Flight system. *Nuclear instruments and methods in physics research.* 960, pp.163629–163629. doi:https://doi.org/10.1016/j.nima.2020.163629.

[27] Mecking, B.A et al (2003). The CEBAF large acceptance spectrometer (CLAS). *Nuclear Instruments and Methods in Physics Research.* [online] 503(3), pp.513–553. doi:https://doi.org/10.1016/S0168-9002(03)01001-5.

[28] Ziegler, V. et al (2020). The CLAS12 software framework and event reconstruction. *Nuclear instruments and methods in physics research.* 959, pp.163472–163472. doi:https://doi.org/10.1016/j.nima.2020.163472.

[29] Anklin, H. et al (1998). Precise measurements of the neutron magnetic form factor. *Physics Letters B*, 428(3-4), pp.248–253. doi:https://doi.org/10.1016/s0370-2693(98)00442-0.

[30] Gerarde, P. G., 2024. *Measuring GMN in CLAS12.* Newport News: s.n. Available at: https://facultystaff.richmond.edu/~ggilfoyl/research/s23GMnTalk.pdf [Accessed June 2024]

[31] Kubon, G. et al (2002). Precise neutron magnetic form factors. *Physics Letters B*, 524(1-2), pp.26–32. doi:https://doi.org/10.1016/s0370-2693(01)01386-7.

[32] Baashen, L., 2023. *Neutron Magnetic Form Factory GMN Measurement at High Q squared with CLAS12,* Miami: Florida International University.

[33] Lachniet, J. D., 2005. *A high precision measurement of the neutron magnetic form factor using the CLAS detector,* Pittsburgh: Carnegie Mellon University

[34] Romanov, D. A., 2024. *Crystal Ball Function,* s.l.: s.n. Available at: https://www.jlab.org/primex/weekly_meetings/slides_2009_07_17/dmitry/crystalball.html [Accessed June 2024]

Chapter 7.

Appendices

Appendix B: CEBAF/CLAS12 additional figures

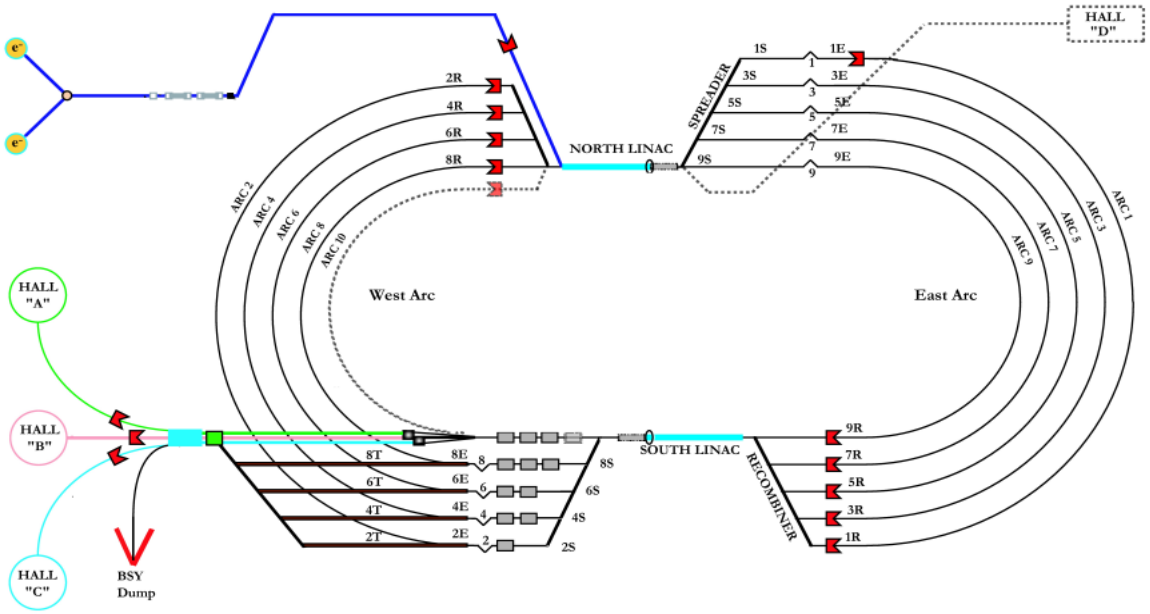

Figure B.1: Top-down figure of CEBAF. Showing in-depth the recirculation performed by the layers of magnetic arcs. Injections, Linacs, and beam switchyard are shown. The path that the electrons take is indicated by the numbers on each arc, the path that they follow proceeds as; 1E-1R-2E-2R-3E-3R-4E-4R-5E-5R-6E-6R-7E-7R-8E-8R-9E-9R-9T(if fully recirculated).

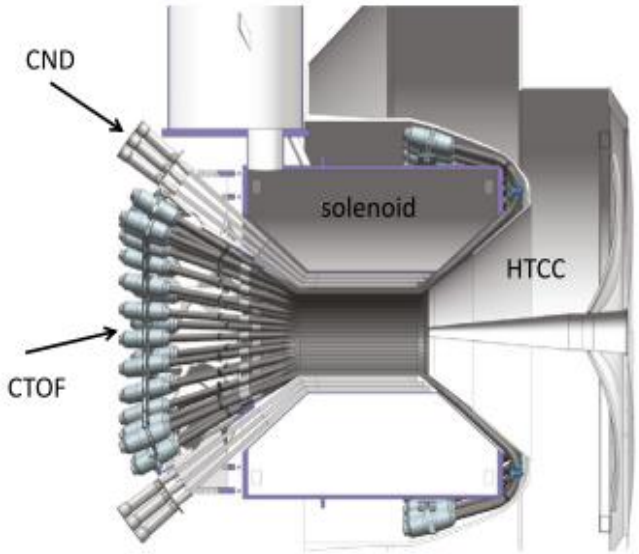

Figure B.2: Central Neutron Detector (CND) and Central time-of-flight (CTOF) detectors shown in poisition around the solenoid, behind the HTCC. from [13].

Appendix C: Additional result plots

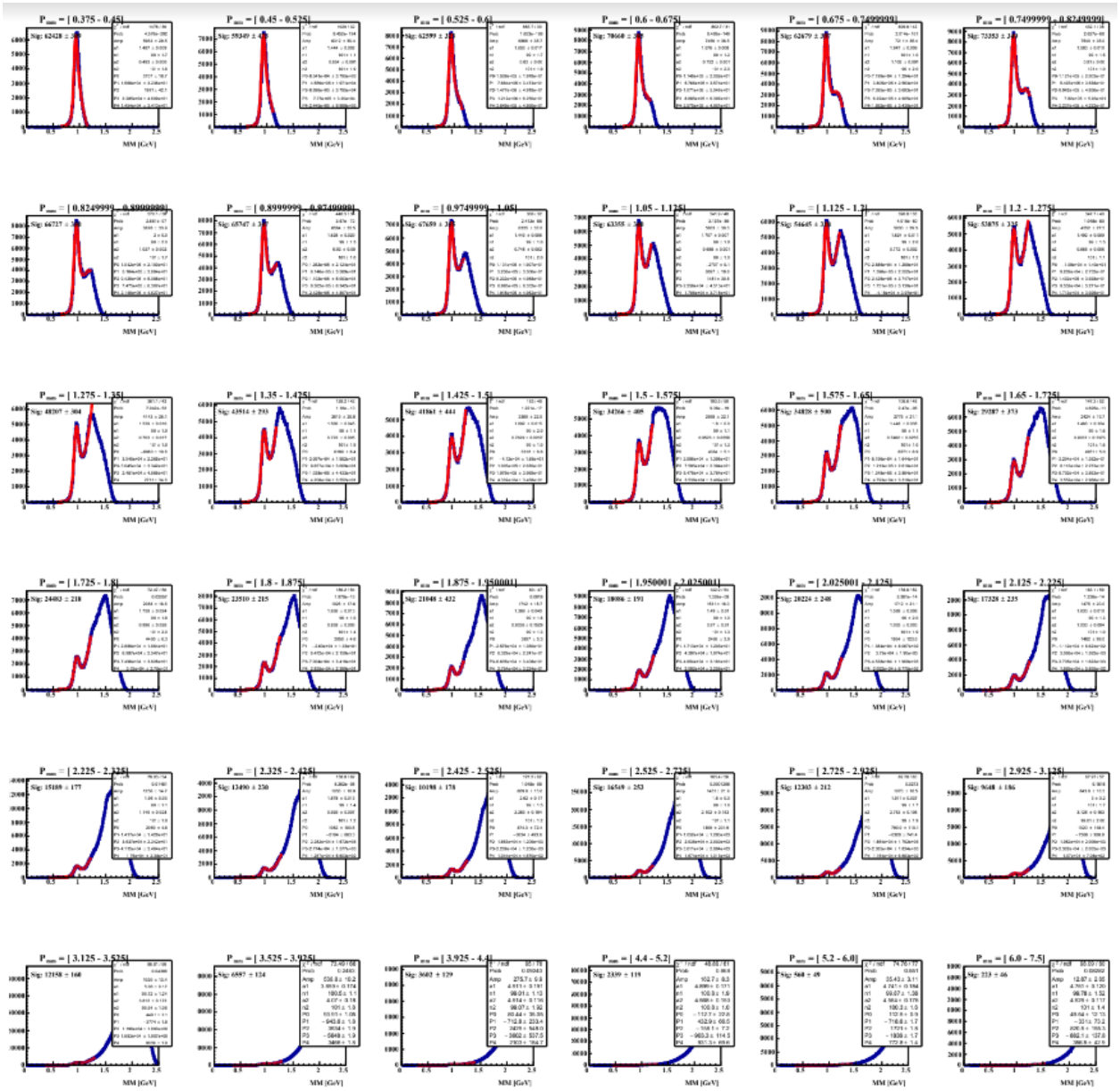

Figure C.1: All 36 Expected bins on one pdf canvas, used for overall viewing of fits and general diagnostics when performing parameterization.

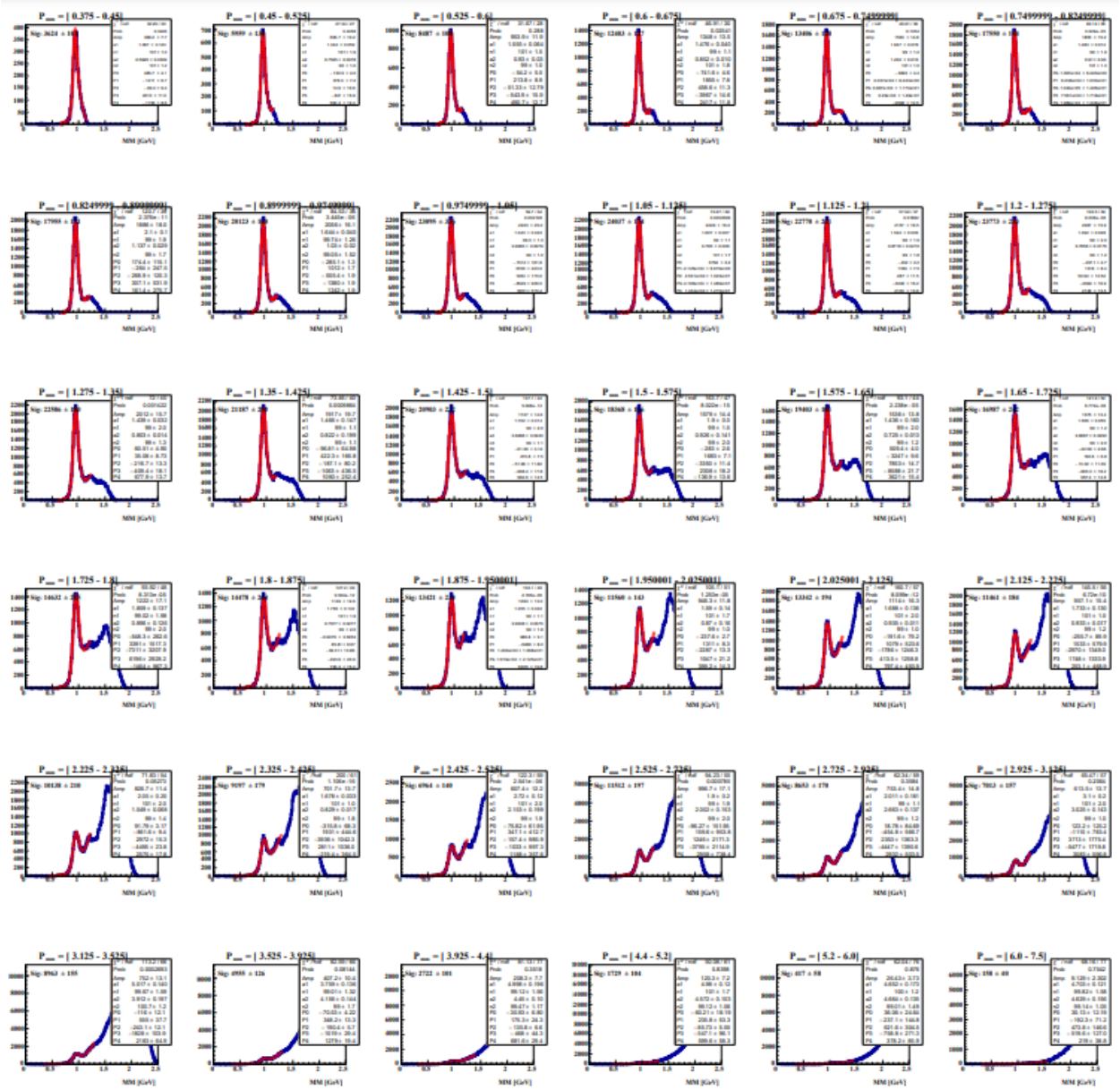

Figure C.2: All 36 Detected bins on one pdf canvas, used for overall viewing of fits and general diagnostics when performing parameterization.